

PL-TR-94-2233

ARCING MITIGATION AND PREDICTIONS FOR HIGH VOLTAGE SOLAR ARRAYS

**Renee L. Mong
James D. Soldi, Jr.
Daniel E. Hastings**

**Massachusetts Institute of Technology
Space Power and Propulsion Laboratory
77 Massachusetts Avenue
Cambridge, MA 02139**

26 July 1994

Scientific Report No. 1

**DTIC
S ELECTE
MAR 20 1995
G D**

Approved For Public Release; Distribution Unlimited



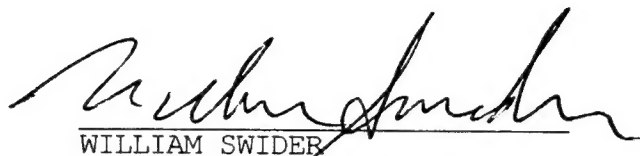
**PHILLIPS LABORATORY
Directorate of Geophysics
AIR FORCE MATERIEL COMMAND
HANSCOM AIR FORCE BASE, MA 01731-3010**

19950317 129

This technical report has been reviewed and is approved for publication.


PAUL S. SEVERANCE
Contract Manager


DAVID A. HARDY
Branch Chief


WILLIAM SWIDER
Deputy Division Director

This report has been reviewed by the ESC Public Affairs Office (PA) and is releasable to the National Technical Information Service (NTIS).

Qualified requestors may obtain additional copies from the Defense Technical Information Center (DTIC). All others should apply to the National Technical Information Service (NTIS).

If your address has changed, or if you wish to be removed from the mailing list, or if the addressee is no longer employed by your organization, please notify PL/IM, 29 Randolph Road, Hanscom AFB, MA 01731-3010. This will assist us in maintaining a current mailing list.

Do not return copies of this report unless contractual obligations or notices on a specific document requires that it be returned.

REPORT DOCUMENTATION PAGE

Form Approved
OMB No. 0704-0188

Public reporting burden for this collection of information is estimated to average 1 hour per response, including the time for reviewing instructions, searching existing data sources, gathering and maintaining the data needed, and completing and reviewing the collection of information. Send comments regarding this burden estimate or any other aspect of this collection of information, including suggestions for reducing this burden, to Washington Headquarters Services, Directorate for Information Operations and Reports, 1215 Jefferson Davis Highway, Suite 1204, Arlington, VA 22202-4302, and to the Office of Management and Budget, Paperwork Reduction Project (0704-0188), Washington, DC 20503.

1. AGENCY USE ONLY (Leave blank)			2. REPORT DATE 26 July 1994	3. REPORT TYPE AND DATES COVERED Scientific No. 1	
4. TITLE AND SUBTITLE Arcing Mitigation and Predictions for High Voltage Solar Arrays			5. FUNDING NUMBERS PE 63410F PR 2822 TA 01 WU PP		
6. AUTHOR(S) Renee L. Mong James D. Soldi, Jr Daniel E. Hastings			Contract F19628-92-K-0016		
7. PERFORMING ORGANIZATION NAME(S) AND ADDRESS(ES) Massachusetts Institute of Technology Space Power and Propulsion Laboratory 77 Massachusetts Avenue Cambridge, MA 02139			8. PERFORMING ORGANIZATION REPORT NUMBER		
9. SPONSORING / MONITORING AGENCY NAME(S) AND ADDRESS(ES) Phillips Laboratory 29 Randolph Road Hanscom AFB, MA 01731-3010			10. SPONSORING / MONITORING AGENCY REPORT NUMBER PL-TR-94-2233		
Contract Manager: Capt Paul Severance/GPSP					
11. SUPPLEMENTARY NOTES					
12a. DISTRIBUTION / AVAILABILITY STATEMENT Approved for public release; distribution unlimited			12b. DISTRIBUTION CODE		
13. ABSTRACT (Maximum 200 words) <p>Future solar arrays are being designed for much higher voltages in order to meet high power demands at low currents. Unfortunately, negatively biased high voltage solar cells have been observed to arc when exposed to the low earth orbit plasma environment. Analytical and numerical models of this arcing phenomenon on conventional solar cells have been developed which show excellent agreement with experimental data. With an understanding of a mechanism for arcing, it is possible to determine methods of arc rate mitigation and to predict arc rates for experiments. Of the various arc rate mitigation methods examined in this research, decreasing the ratio of coverglass/adhesive dielectric constants and overhanging the coverglass show the most promise in reducing or even eliminating arcing. In addition, arcing rates were predicted for the high voltage biased arrays of the Air Force's Photovoltaic Array Space Power Plus Diagnostics experiment (PASP Plus). These predictions provide both expectations for the mission and a means to test the numerical and analytical models in the space environment for different solar cell technologies. Finally, a numerical model of the arc initiation process was also developed for wrap-through-contact cells.</p>					
14. SUBJECT TERMS Solar array arcing High voltage solar arrays Wrap-through-contact solar cells			Space environmental interactions PASP Plus		15. NUMBER OF PAGES 82
16. PRICE CODE					
17. SECURITY CLASSIFICATION OF REPORT Unclassified	18. SECURITY CLASSIFICATION OF THIS PAGE Unclassified	19. SECURITY CLASSIFICATION OF ABSTRACT Unclassified	20. LIMITATION OF ABSTRACT SAR		

Accession For	
NTIS	CRA&I <input checked="" type="checkbox"/>
DTIC	TAB <input type="checkbox"/>
Unannounced <input type="checkbox"/>	
Justification _____	
By _____	
Distribution / _____	
Availability Codes	
Dist	Avail and / or Special
A-1	

Contents

1	Introduction	1
1.1	Background	2
1.2	Overview of This Research	8
2	Numerical and Analytical Models	9
2.1	Conventional Solar Cells	9
2.1.1	Numerical Model	9
2.1.2	Analytical Model	15
2.2	Wrap-Through-Contact Cells	21
3	Arc Mitigation Methods	30
3.1	Control Case	30
3.2	Interconnector Material	33
3.3	Dielectric Thickness	33
3.4	Secondary Electron Yield	36
3.5	Dielectric Constants	37
3.6	Overhanging the Coverglass	42
3.6.1	Numerical Results	42
3.6.2	Analysis	46
3.7	Arc Rate Results	49
4	PASP Plus Predictions	53
4.1	PASP Plus	53
4.2	Experiment Description	54
4.3	Predictions	56
5	Conclusions	67

List of Figures

1	Schematic of a conventional solar cell	2
2	Model of the conventional solar array used for numerical simulations	5
3	Arcing sequence of a high voltage solar array	6
4	Model system of the high voltage solar array and plasma interactions	10
5	Grid structure for conventional cell calculations	11
6	Typical electric potential contour plot for ambient ion charging of conventional cells	13
7	Typical surface charge density along side dielectrics after ambient ion charging of conventional cells	13
8	Electric field lines over a whisker on conductor surface	14
9	Geometry for EFEE charging	16
10	Typical electric field run-away versus time	17
11	Experimental data for ground and flight experiments	20
12	Schematic of a wrap-through-contact solar array	21
13	Wrap-through-contact solar array model used for numerical simulations	22
14	Typical grid structure for calculations	23
15	Typical electric potential for ambient ion charging of WTC cells	24
16	Typical surface charge density along the side dielectric surface after ambient ion charging of WTC cells	25
17	Class 1 electric field at upper triple junction versus time	26
18	Class 2 electric field at upper triple junction versus time	27
19	Class 1 surface charge density over the coverglass (a) side surface, (b) front surface	28
20	Class 2 surface charge density over the coverglass side surface	29
21	Enhanced field electron emission charging time, τ_{efee} , versus βV for the silicon conventional control case	32
22	Analytic arc rates for the silicon conventional control case	32

23	Enhanced field electron emission charging time, τ_{efee} , versus βV for different work functions, ϕ_w (eV)	34
24	Analytic predictions and numerical results for $\tau_{efee}/\tau_{efee}(\phi_w = 4.76\text{eV})$ versus βV	34
25	Enhanced field electron emission charging time, τ_{efee} , versus βV for different dielectric thicknesses, $d(\mu\text{m})$	35
26	Analytic predictions and numerical results for $\tau_{efee}/\tau_{efee}(d = 190\mu\text{m})$ versus βV	36
27	Enhanced field electron emission charging time, τ_{efee} , versus βV for different secondary electron yields, γ_{ee}	37
28	Surface charge density as a function of distance from the triple junction for different secondary electron yields, γ_{ee}	38
29	Enhanced field electron emission charging time, τ_{efee} , versus βV for different dielectric constant ratios	39
30	Dielectric side surface charge density before EFEE charging for different dielectric constants	40
31	Electron trajectories for $\epsilon_{d_1}/\epsilon_{d_2} = 2.7$	41
32	Electron trajectories for the control case of $\epsilon_{d_1}/\epsilon_{d_2} = 1.3$	41
33	Electron trajectories for $\epsilon_{d_1}/\epsilon_{d_2} = 0.74$	42
34	Average secondary electron yield over the adhesive versus time for different dielectric constants	43
35	Model of coverglass overhang	43
36	Enhanced field electron emission charging time, τ_{efee} , versus βV for different overhang lengths	44
37	Class comparison of τ_{efee} versus E_{TJ} for $\beta V = 3.5 \times 10^5\text{V}$	45
38	Electron trajectories for $10\mu\text{m}$ overhang; $\beta V = 3 \times 10^5\text{V}$	45
39	Electron trajectories for $50\mu\text{m}$ overhang; $\beta V = 3 \times 10^5\text{V}$	46
40	Class 1 dielectric surface potential; $\beta V = 3 \times 10^5\text{V}$, $d_o = 10\mu\text{m}$	47
41	Class 2 dielectric surface potential; $\beta V = 3.25 \times 10^5\text{V}$, $d_o = 50\mu\text{m}$	47
42	Analytic arc rates for varying interconnector work functions, ϕ_w	50
43	Analytic arc rates for varying dielectric thicknesses, d	50
44	Predicted arc rates for varying secondary electron yields, γ_{ee}	51
45	Predicted arc rates for varying dielectric constant ratios, $\epsilon_{d_1}/\epsilon_{d_2}$	52
46	Predicted arc rates for varying coverglass overhang lengths, d_o (μm)	52
47	Deployed APEX spacecraft with PASP Plus experiment payload	55

48	Selected arc rate predictions with standard deviation errors for Si conventional array #1	60
49	Complete arc rate predictions in the differentiating voltage range for Si array #1	60
50	Selected arc rate predictions with standard deviation errors for Si conventional array #2	61
51	Complete arc rate predictions in the differentiating voltage range for Si array #2	61
52	Selected arc rate predictions with standard deviation errors for GaAs/Ge conventional array #4	62
53	Complete arc rate predictions in the differentiating voltage range for GaAs/Ge array #4	62
54	Selected arc rate predictions with standard deviation errors for GaAs/Ge conventional array #6	63
55	Complete arc rate predictions in the differentiating voltage range for GaAs/Ge array #6	63
56	Selected arc rate predictions with standard deviation errors for GaAs/Ge conventional array #11	64
57	Complete arc rate predictions in the differentiating voltage range for GaAs/Ge array #11	64
58	Selected arc rate predictions with standard deviation errors for APSA (#36)	65
59	Complete arc rate predictions in the differentiating voltage range for APSA (#36)	65
60	Arc rate prediction comparison for all PASP Plus conventional arrays at 350km	66

List of Tables

1	Conventional silicon cell data used in numerical simulations	31
2	PASP Plus data used for arc rate predictions	57

List of Symbols

A	Fowler Nordheim coefficient ($1.54 \times 10^{-6} \times 10^{4.52\phi_W^{-1/2}} / \phi_W$ A/V ²)
B	Fowler Nordheim coefficient ($6.53 \times 10^9 \phi_W^{1.5}$ V/m)
C_{diele}	capacitance of dielectric (F/m ²)
C_{front}	capacitance of coverglass front surface (F)
d	thickness of dielectric (m)
d_1	thickness of coverglass (m)
d_2	thickness of adhesive (m)
d_{gap}	gap distance between cathode and anode (m)
d_i	distance of electron first impact point from triple junction (m)
d_o	overhang distance of coverglass (m)
d_o^c	critical overhang distance of coverglass (m)
E_ϵ	electric field at emission site (V/m)
E_i	electron incident energy on dielectric plate (eV)
E_{max}	electron incident energy for maximum secondary electron yield (eV)
E_{TJ}	electric field at triple junction (V/m)
E_1	electric field of coverglass (V/m)
E_2	electric field of adhesive (V/m)
j_{ec}	electron current density from conductor (A/m ²)
j_{ee}	secondary electron current density from dielectric (A/m ²)
j_{FN}	Fowler-Nordheim current density from the conductor (A/m ²)
j_{id}	ion ram current density to the dielectric (A/m ²)
n_ϵ	plasma number density (m ⁻³)
n_{es}	emission site number density (m ⁻²)
m_ϵ	electron mass (kg)
m_i	ion mass (kg)
\dot{R}	arc rate (sec ⁻¹)
r_s	sheath radius (m)
S_{FN}	emission site area determined from F-N plot (m ²)

S_{real}	emission site area determined by accounting for electron space charge effects (m^2)
T_e	electron temperature (eV)
T_i	ion temperature (eV)
V_{arc}	voltage at which last arc occurred V
V_{bias}	bias voltage of interconnector/conductor V
V_e	voltage which minimizes arcing time V
V_i	initial voltage before solar cell charging V
v_{ion}	mean speed of ions entering sheath (m/sec)
v_x	electron velocity in the x direction (m/sec)
v_y	electron velocity in the y direction (m/sec)
y	distance of emission site from the triple junction (m)
β	field enhancement factor
ΔQ	charge lost from one coverglass by one discharge (C)
ϵ_{d_1}	relative dielectric constant of coverglass
ϵ_{d_2}	relative dielectric constant of adhesive
\mathcal{E}_1	energy at $\gamma_{ee} = 1$ (eV)
ϕ_c	potential of conductor (V)
ϕ_i	potential of coverglass-adhesive interface (V)
ϕ_w	work function (eV)
γ_{ee}	secondary electron yield
γ_{max}	maximum secondary electron yield at normal incidence
η	factor accounting for difference in electric field at emission site and triple junction
θ_i	incident impact angle of electron onto the dielectric surface
σ	surface charge density (C/m^2)
τ_{arc}	time between arcs (sec)
$\tau_{e\text{fee}}$	EFEE charging time (sec)
τ_{ion}	ion charging time (sec)
τ_{exp}	experiment time (sec)
ξ	factor accounting for difference of dielectric constants between coverglass and adhesive

Chapter 1

Introduction

In the past and present, solar arrays used in space have been operating at low voltage levels, typically at 28V. Future solar arrays, however, are being designed for much higher voltages in order to meet high power demands of the order of 10kW to 1MW. High current levels could be used instead to achieve these increased power demands, but the power distribution cables would need to be more massive and the resistive losses would be greater. Consequently, the current is maintained at a low value while the voltage is increased to attain the necessary power level.

A schematic of a conventional solar cell is shown in Figure 1. The coverglass and substrate shield the solar cell from the environment, mainly to reduce radiation degradation. These are attached to the cell with adhesives. The solar cell itself is a semiconductor of two parts, a p-type semiconductor which has an abundance of electrons and an n-type semiconductor which has an abundance of electron holes. This construction allows the solar cell to use the photoelectric effect to convert solar energy into electric power. A photon with energy equal to or greater than the energy gap of the solar cell it enters will free an electron. This creates an electron-hole pair. If the pair is in the p-type semiconductor, the electron will be accelerated across the p-n barrier to the n-type semiconductor where it will recombine. The hole, however, will be repelled by the barrier because of the excess of holes in the n-type semiconductor. Likewise, if the electron-hole pair is in the n-type semiconductor, the hole will be accelerated across the p-n barrier and the electron repelled. Consequently, metal interconnectors connect the n-type semiconductor of one cell to the p-type semiconductor of the adjacent cell to utilize the current created by the electron and hole movement. Solar cells are connected in parallel with metal interconnectors to obtain desired current levels and connected in series to obtain desired voltage levels.

The solar array, along with other surfaces of the spacecraft which can allow the passage of current, collects current from the ambient plasma. In steady state, the spacecraft is grounded

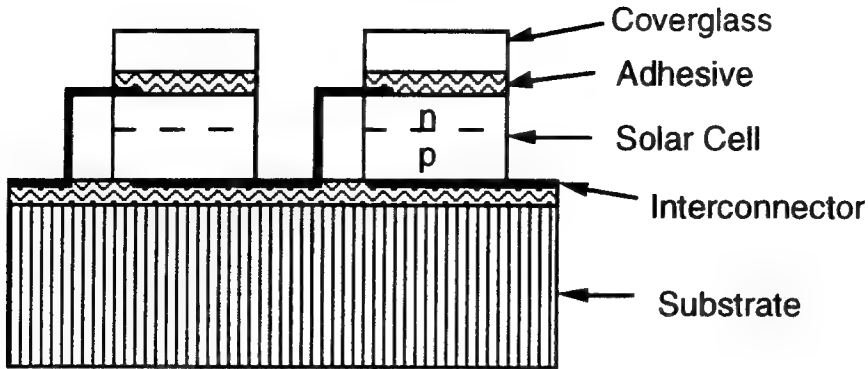


Figure 1: Schematic of a conventional solar cell

with respect to the plasma by the zero net charging condition

$$\frac{\partial \rho}{\partial t} + \nabla \vec{j} = 0, \quad (1)$$

which is derived from Ampere's Law and Gauss's Law. To obey this condition, most of the solar array floats negatively with respect to the plasma. This is because the random thermal flux of the lighter electrons to the spacecraft is greater than the random flux of the heavier ions. Therefore, the spacecraft surfaces must be at a negative potential in order to maintain zero net current collection.

High-voltage solar arrays, however, have been observed to interact with the plasma environment of low earth orbit in two undesirable manners. For positive voltages, the current collection can be anomalously large, possibly leading to surface damage²⁵. This phenomenon, known as "snapover", occurs when the dielectric surface potential becomes positive, attracting electrons. Above a certain potential, more than one secondary electron is released by the incident electrons. These excessive secondary electrons are collected by the interconnector and seen as a current increase, which then incurs a power loss. For large negative voltage operation, arc discharges can occur¹¹. Arcing observed in experiments has been defined as a sharp current pulse much larger than the ambient current collection which lasts up to a few microseconds. This current pulse is usually accompanied by a light flash at the edge of the solar cell coverglass. Arc discharges can cause electromagnetic interference and solar cell damage²⁶, so there is a need to study mitigation methods and to be able to predict arcing rates with models.

1.1 Background

Arcing has been studied in many experiments and theoretical arguments. The Plasma Interactions Experiments (PIX I and II) and Solar Array Module Plasma Interactions Experiments

(SAMPIE) have been the only space experiments so far, though several more space experiments are planned for the near future. Arcing has also been observed in many ground tests conducted in vacuum plasma chambers. Two different theoretical explanations were given by Parks et al.²¹ and Hastings et al.¹⁰. Cho and Hastings³ used ideas from both to present a more complete theory of the arcing sequence of events.

Arcing on solar cells was originally observed by Heron et al.¹¹ in 1971 during a high voltage solar array test in a plasma chamber. The array was biased to -16kV, and arcing was observed as low as -6kV in a plasma density of 10^8 m^{-3} .

In 1978, the first Plasma Interactive Experiment (PIX)⁶ confirmed that arcing occurs in space. As an auxilliary payload on Landsat 3's Delta launch vehicle, PIX operated for 4 hours in a polar orbit around 920km. A solar array of twenty-four 2cm \times 2cm conventional silicon cells was externally biased to -1000V. Arcing discharges began at -750V.

In 1983, PIX II⁷ was launched also as an auxilliary payload aboard a Delta launch vehicle into a near circular polar orbit of approximately 900km in altitude. The 500 2cm \times 2cm silicon conventional cells, biased to -1000V, experienced arcing as low as -255V and at densities as low as 10^3 cm^{-3} . The results also found arcing to be the most detrimental effect of negative biasing.

Ferguson⁴ studied the PIX II ground and flight results. The interconnectors collected current proportional to the applied voltage bias. The arc rate \dot{R} was determined to scale as

$$\dot{R} \approx n_e \left(\frac{T_i^{1/2}}{m_i^{1/2}} \right) V_{bias}^a, \quad (2)$$

where $a \approx 5$ for the ground experiments and $a \approx 3$ for the flight experiments, n_e is the ambient plasma number density, T_i is the ambient ion temperature, and m_i is the ambient plasma ion mass. The dependence of the arc rate on these parameters indicates that the coverglass surface is recharged by the thermal flux of ions.

Ground experiments revealed more characteristics of the arcing phenomenon. Experiments by Fujii et al.⁵ showed that dielectric material near the biased conductor in the plasma environment is essential for arcing to occur. Fujii et al. tested material plates biased to high negative voltages in a plasma environment. The plate partially covered by a 200 μm thick coverglass experienced arcing at -450V while the uncovered plate did not arc, except at -1000V when the arc occurred at the substrate. Snyder²² measured the electric potential on the coverglass and found that it decreased significantly when an arc occurred. This indicates that the negative charge created during arcing discharged the positive surface charge accumulated on the coverglass surface. Both Snyder and Tyree²³ and Inouye and Chaky¹⁵ observed electron emission from the solar array that could not be explained by the ambient

plasma. Finally, electromagnetic waves generated from the arcing current were measured by Leung¹⁹.

The first theoretical model was proposed by Jongeward et al.¹⁶ and later expanded by Parks et al.²¹. Jongeward et al. attributed Snyder's²² experimental observation of the decrease in coverglass potential prior to arcing to enhanced electron emission from the interconnector, which corresponds to the electron emission observed in References 23 and 15. They suggested the emission is due to a thin layer of ions deposited on the interconnector, causing the electric field to be significantly increased. The time for positive charge build up is then dependent on the ambient density n_e , the interconnector size, and the bias voltage. The arc discharge is proposed to occur by a positive feedback mechanism from electron heating which leads to a space charge limited discharge. At low ion densities, other surface neutralizing effects are said to dominate, thus inhibiting the positive charge build up. Jongeward et al. also modeled the arc discharge decay time by assuming space charge limited conditions and showed that the peak current magnitude agrees well with this assumption.

Parks et al.²¹ concentrated on further detailing the theory proposed by Jongeward et al.¹⁶ on the prebreakdown electron emission current. They accepted Jongeward's theory of positive charge build-up in a thin insulating layer on the interconnector and of arcing originated from interconnector electron emission instead of from the ambient plasma. Parks et al. proposed the addition of the phenomena presented by Latham^{17,18}, namely that non-metallic emission processes are significantly responsible for electron emission by nominally metallic surfaces. Therefore, Parks et al. claimed that the arc rate must be proportional to the electron emission current density and the bias voltage. They further suggested that electron emission is controlled by the vacuum electric field at the surface of the insulator. Given these assumptions, they determined that the rate of field build-up in the insulator is

$$\epsilon_0 \frac{d}{dt} (\epsilon_{ins} E_{ins} - E_{ins-vac}) = j_i + j_{FN} (e^{ad} P - 1), \quad (3)$$

where ϵ_{ins} is the dielectric constant of the insulator layer, E_{ins} is the electric field inside the insulator, $E_{ins-vac}$ is the electric field at the insulator-vacuum interface, j_i is the ion current density, j_{FN} is the Fowler-Nordheim emission current at the metal-insulator interface, a is the rate of ionization per unit distance inside the layer, d is the thickness of the insulator layer, and P is the probability that electrons are emitted from the insulator-vacuum interface. The emission current from the metal-insulator interface is given by

$$j_{FN} = A E_{ins}^2 e^{-\frac{B}{E_{ins}}}, \quad (4)$$

where A and B are the Fowler-Nordheim emission coefficients, given in Eq. (8) and (9). This

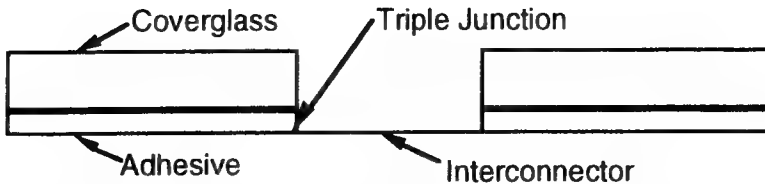


Figure 2: Model of the conventional solar array used for numerical simulations

expression for the electric field accounted for experimental observations of the characteristics of the voltage threshold, the prebreakdown electron emission current, and the arcing rate.

Hastings et al.¹⁰ did not try to explain the prebreakdown electron emission current but instead proposed a model for the gas breakdown seen as the arc discharge. They suggested that neutral gas is desorbed from the sides of the coverglass by electron bombardment, a phenomena known as electron stimulated desorption (ESD). The bombarding electrons are emitted from the interconnector, as determined from Snyder's experiments²², and from the coverglass as secondary electrons which return to the side surface. The desorbed neutrals then accumulate in the gap between the coverglasses over the interconnector, forming a potentially high-pressure gas layer which can break down from the electron emission current flowing through it. This was in contrast to the previous theory which suggested that the arc occurs in an insulator on the surface of the interconnector.

Recent work by Cho and Hastings³ combined some of the ideas from these two theories and studied the charging of the region near the plasma, dielectric, and conductor triple junction. The model that they studied is shown in Figure 2. The dielectric consists of both the coverglass and the adhesive bonding the coverglass to the solar cell. The conductor is the interconnector, which is usually placed between the cell and substrate on one end and between the cell and cover adhesive in the adjoining cell. The solar cell itself was neglected since the potential drop across it is at most a few volts while the potential drop across the coverglass and adhesive is hundreds or even thousands of volts for high voltage operation.

Cho and Hastings developed a numerical simulation of the arc initiation processes. They studied charging of the dielectric surfaces by three sources: ambient ions, ion-induced secondary electrons, and enhanced field electron emission. From numerical results, they determined the following arc sequence, illustrated in Figure 3:

- (1) ambient ions charge the dielectric front surface, but leave the side surface effectively uncharged;
- (2) ambient ions induce secondary electrons from the conductor which charge the side surface to a steady state unless enhanced field electron emission (EFEE) becomes significant;

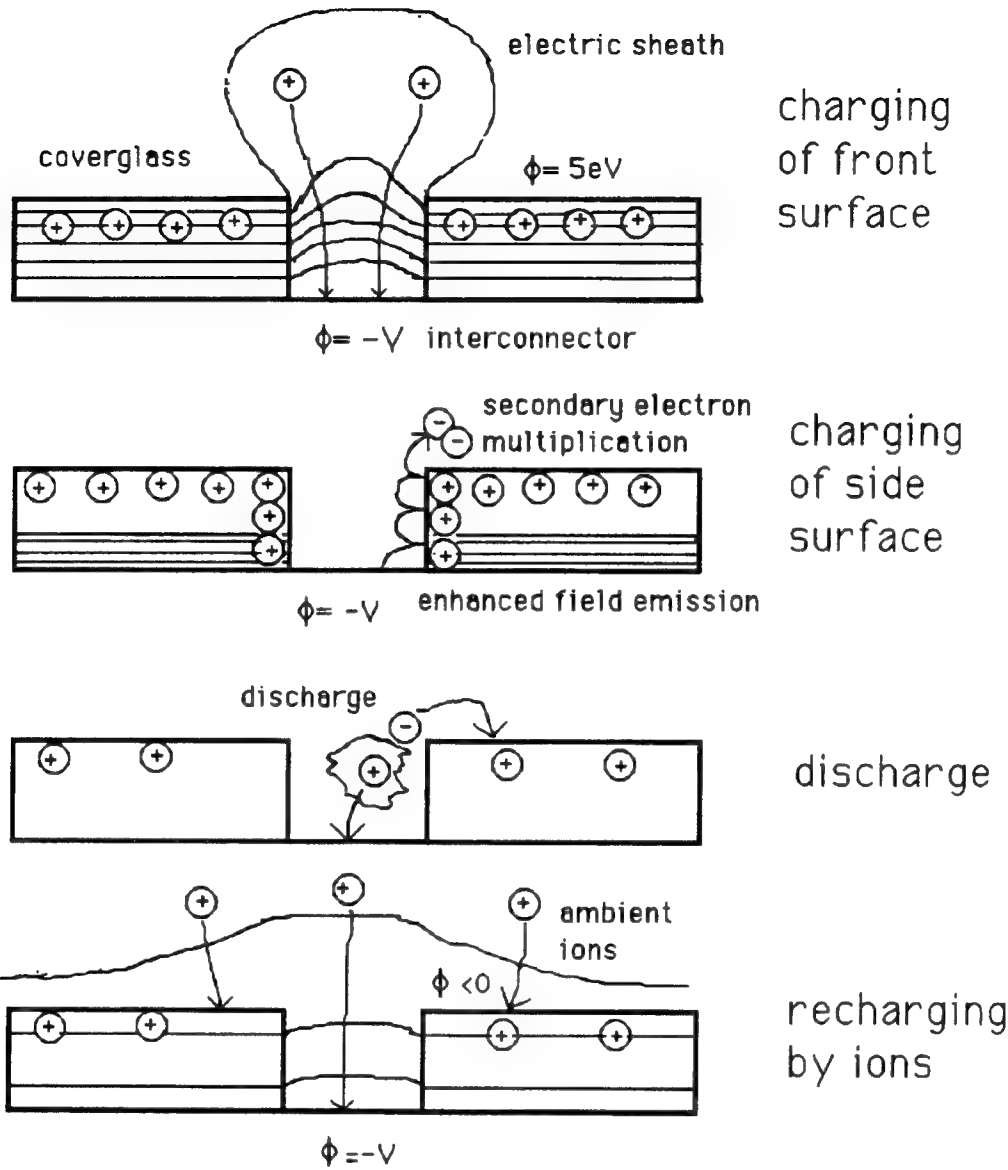


Figure 3: Arcing sequence of a high voltage solar array

- (3) EFEE will charge the side surface if there is an electron emission site close to the triple junction with a high field enhancement factor, β ; and
- (4) EFEE can result in collisional ionization of neutrals desorbed from the coverglass, which is what is observed as the arc discharge.

They also found that the electric field at the triple junction is not bounded during EFEE charging.

Cho and Hastings used the numerical results to develop analytical formulas describing the arcing rate^{3,9}. They suggested that the time between arcs is the minimum of the sum

of the ambient charging time τ_{ion} and the enhanced field electron emission charging time τ_{efee} , so that the arc rate \dot{R} is given by:

$$\dot{R} = \min(\tau_{ion} + \tau_{efee})^{-1} \quad (5)$$

For the ion charging, Cho and Hastings showed that ambient ions mainly charge the front surfaces of the coverglass, not the side surfaces. They expressed this time as

$$\tau_{ion} = \frac{\Delta Q}{en_e v_{ion} A_{cell}}, \quad (6)$$

where ΔQ is the charge lost by the coverglass due to an arc discharge, which must be recovered; $en_e v_{ion}$ is the ambient ion flux to the front surfaces, with v_{ion} as the mean speed of ions entering the sheath surrounding the solar array; and A_{cell} is the frontal area of the coverglass. Assuming a constant secondary electron yield and constant voltage bias, they derived the following analytical expression for the EFEE charging time, τ_{efee} :

$$\tau_{efee} = \frac{C_{diele} d_i^2}{(\gamma_{ee} - 1) \sqrt{S_{real}} \eta \xi A \frac{S_{FN}}{S_{real}} B \beta} \exp\left(\frac{Bd}{\beta V \eta \xi_0}\right), \quad (7)$$

where A and B are the Fowler-Nordheim coefficients given by

$$A = \frac{1.54 \times 10^{-6} 10^{4.52/\sqrt{\phi_w}}}{\phi_w}, \quad (8)$$

$$B = 6.53 \times 10^9 \phi_w^{1.5}, \quad (9)$$

ξ is a factor to account for the difference in dielectric constants and is given by

$$\xi = \left[\frac{d_2}{d_i} + \frac{\epsilon_{d_2}}{\epsilon_{d_1}} \frac{(d_i - d_2)}{d_i} \right]^{-1}, \quad (10)$$

ξ_0 is ξ evaluated with $d_i = d$, d_i is the distance from the triple junction of the first impact by an electron emitted from the conductor, C_{diele} is the capacitance of the dielectric at this impact site, γ_{ee} is the secondary electron yield of the dielectric, S_{real} is the real area of the emission site, S_{FN} is the Fowler-Nordheim “effective” area of the emission site, η is a factor to account for the difference in the electric field at the emission site from the triple junction, d_1 is the thickness of the coverglass, d_2 is the thickness of the adhesive, $d = d_1 + d_2$, V is the voltage at which the arc occurs, and β is the field enhancement factor. From comparison with experiments, Hastings et al.⁹ suggested that β must be greater than a few hundred, so they assumed that the field enhancement is due to a thin dielectric layer on the conductor surface rather than microprotrusions. They later updated their views as explained in Section 2.1.1.

From experimental observations, Hastings et al.⁹ suggested other characteristics of the arcing processes, such as the discharge wave hypothesis and the occurrence of one arc at a time within a certain area. The discharge wave hypothesis suggested that at arc initiation emitted electrons form a plasma cloud over the solar array. Some of the electrons, attracted by the positive surface potential, strike the coverglasses in the local area until they are discharged. Experimental results also showed that the arc current is more likely to be carried by electrons, consistent with the hypothesis that arcing is initiated by electron emission from the interconnector. In addition, as the temperature increased fewer neutral gas molecules were desorbed from the dielectrics and the arc rate was seen to decrease, consistent with the hypothesis that ionization of the neutral gases also plays a role in arc initiation.

1.2 Overview of This Research

Power requirements for space systems are increasing significantly. As the most reliable power source, high voltage solar arrays will be needed to meet these requirements. Since arcing degrades the array performance and causes electromagnetic interference which affects nearby instruments, it is imperative to study arcing. Recent studies by Cho and Hastings^{3,9} determined an arcing sequence of events and an arcing rate based on numerical and theoretical work which has been shown to agree well with experimental results. With these models it is possible to determine methods of arc rate mitigation and to predict arc rates for experiments. This research can then be used in the design of new solar cells and in the design of high voltage solar arrays.

The focus of this research is twofold: to identify and study mitigating effects on arc rates and to present arc rate predictions for the Air Force's Photovoltaic Array Space Power Plus Diagnostics (PASP Plus) experiment. In Chapter 2, the numerical and analytical models developed by Cho and Hastings are reviewed, and the numerical model modified for the wrap-through-contact solar cell geometry is presented. Based on the analytical model for conventional solar cells, arc rate reduction methods are studied using the corresponding numerical model in Chapter 3. In Chapter 4, arcing rates are predicted for the high-voltage biased arrays of the PASP Plus experiment. Finally, conclusions are summarized in Chapter 5.

Chapter 2

Numerical and Analytical Models

2.1 Conventional Solar Cells

A schematic of a conventional solar cell is shown in Figure 1. In high voltage operation, the voltage differential over the coverglass and adhesive can be hundreds or even thousands of volts while the voltage differential over the cell itself is at most a few volts. For modeling purposes, the cell semiconductor can therefore be neglected, as shown in Figure 2. In this model, the interconnector is a conductor and the coverglass and adhesive are dielectrics. The numerical and analytical models used for conventional cells were developed by Cho and Hastings^{3,9}, as briefly described in Section 1.2.

2.1.1 Numerical Model

The numerical model incorporates all relevant physical characteristics and processes for solar cell charging from the ambient plasma, electron emission from the interconnector, and secondary electron emission from the dielectrics. A representation of this system is shown in Figure 4. The coverglass and adhesive surface charge densities are affected by the ion ram current density j_{id} , the electron emission current density from the conductor j_{ec} , and the secondary electron current density from the surface j_{ee} . After arc initiation, the current densities from the ionization of neutral gases may also be significant. These are not considered, however, as only the time to arc initiation is the focus of this research. The rate of change of the dielectric surface charge density can then be expressed as

$$\frac{d\sigma}{dt}(x, t) = j_{id}(x, t) - \int P(x, y, t)j_{ec}(y, t)dy - \int P(x, x', t)j_{ee}(x')dx' + j_{ee}(x, t). \quad (11)$$

where $P(x, y, t)$ is the probability that an electron emitted from position y on the conductor hit the dielectric at position x at time t , and $P(x, x', t)$ is the probability that an electron emitted at x' hits the dielectric at x .

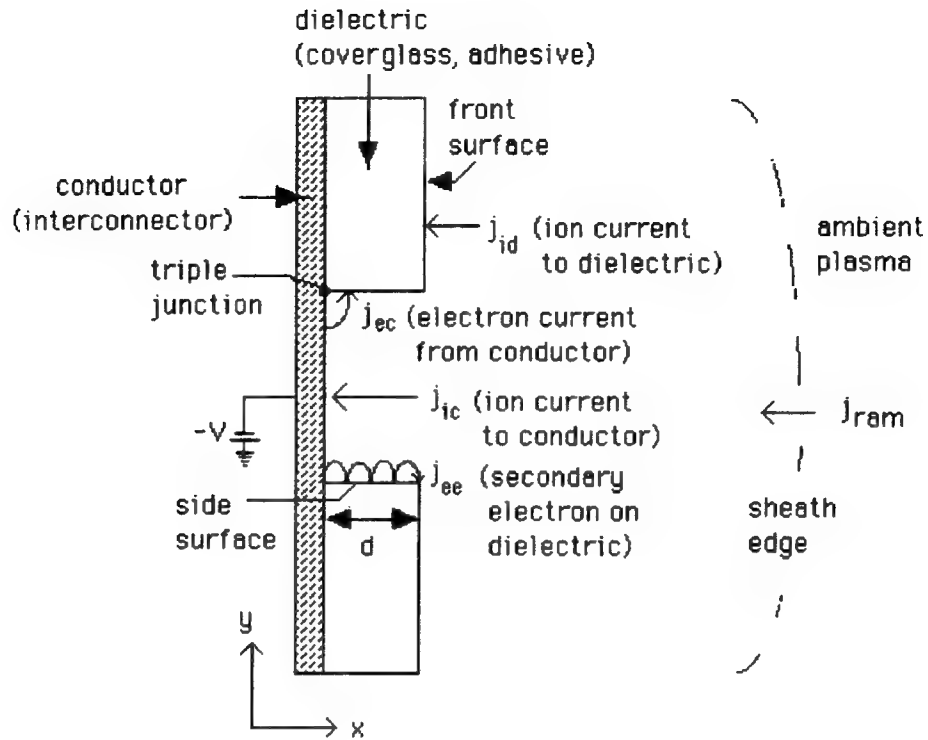


Figure 4: Model system of the high voltage solar array and plasma interactions

The numerical model consists of three schemes. The first scheme uses the capacitance matrix method to obtain a preliminary electric potential distribution along the dielectric surfaces. The second scheme involves a particle-in-cell (PIC) method which is used for ambient ion charging. Once a steady state is obtained from the ion charging, a space-charge-free orbit integration scheme calculates the electron charging by enhanced field electron emission (EFEE).

All schemes use the same computational domain and grid. The phase space of the domain consists of two position coordinates and three velocity coordinates. As shown in Figure 5, the domain includes two halves of solar cells with the interconnector forming the lower boundary of the gap between the cells. The boundary condition far from the cells at $x = 0$ is $\phi = 0$, simulating the far field. In these simulations, any electrons leaving the domain at $x = 0$ will also leave the sheath. The boundaries are thus Dirichlet in the x direction and periodic in the y direction to simulate a solar array. The grid is clustered along the dielectric sides and near the interconnector for better resolution of the large electric potential gradients in these areas.

The capacitance matrix method is used to obtain an initial condition for the PIC code, thus reducing the simulation time. In employing this method, which is given in Reference

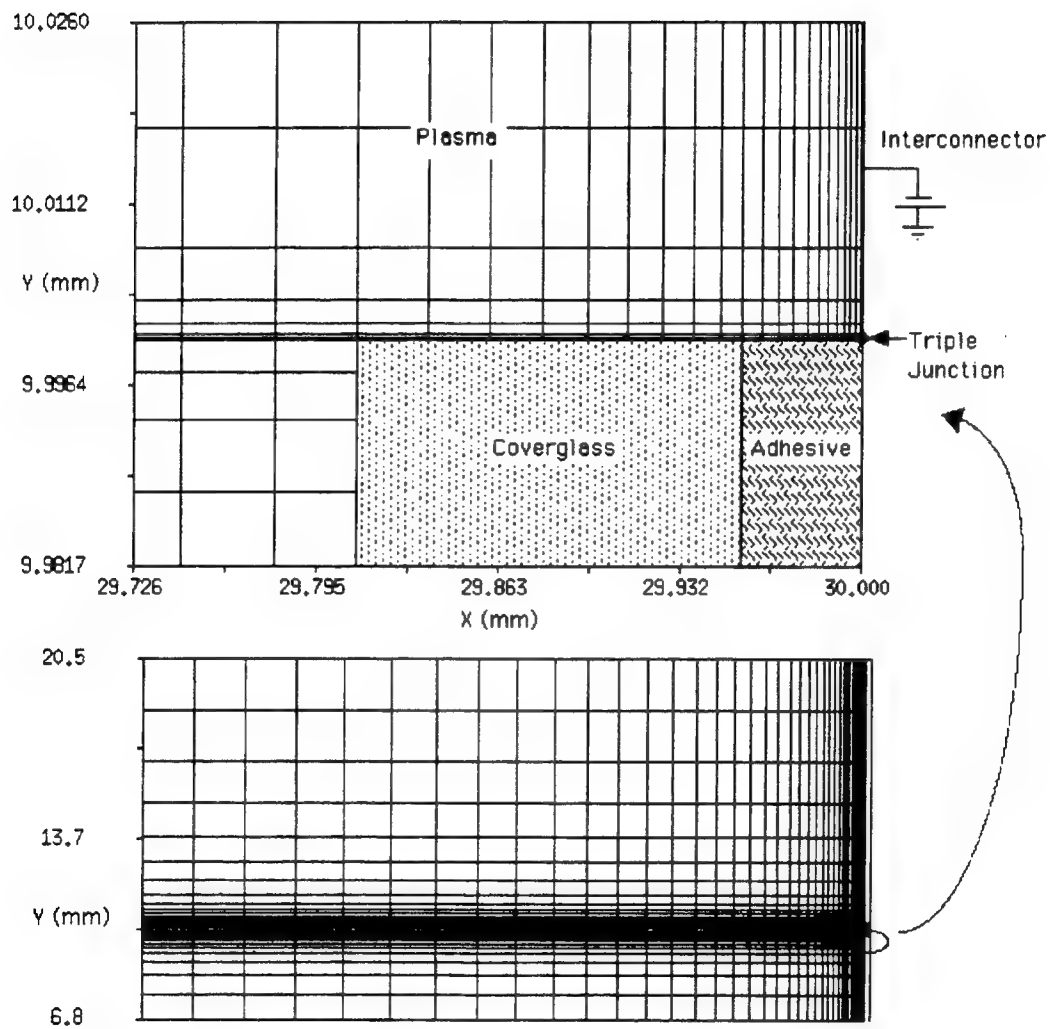


Figure 5: Grid structure for conventional cell calculations

14, a unit charge is ascribed to one cell on the dielectric surface while all other cells have zero charge. The Poisson equation is then solved to determine the electric potential in every cell on the dielectric surface due to this unit charge. This process is repeated for each grid cell along the surface of the dielectrics. Afterwards, the array containing all of the potential values calculated is inverted to determine the capacitance value for each grid cell. This matrix is stored for use as the initial conditions of the PIC code, so that the simulation can be started from any charging state described by only the surface charge or the surface potential.

With the capacitance matrix calculated for unit charges, the PIC code calculates the space potential based on a pre-determined surface potential. The initial conditions for the dielectric potential are $\phi = 0$ on the front surface and a linear distribution of ϕ on the side surface with the conductor voltage at one end and the front surface zero voltage at the other end. The ram velocity is oriented 90° to the dielectric front surfaces and conductor. To save computational time, an artificial ion mass is used such that $m_i/m_e = 100$. Ions and electrons are initially inserted uniformly throughout the domain according to the ambient density. After the space potential is calculated using the Poisson equation, the ions and electrons are moved according to the new potential. A new space charge density for each grid point can then be calculated based on the new ion and electron positions. This loop is then repeated with the potential being re-calculated based on the new charge density. The PIC code is run for a time equivalent to the inverse of the ion plasma frequency to adjust the space charge completely with the surface potential.

The results from the PIC scheme are the initial conditions for the dielectric charging scheme. A typical contour plot of the initial electric potential is shown in Figure 6, and the corresponding surface charge density is shown in Figure 7.

No electron emissions from the conductor or dielectric are taken into account in the PIC code since they are negligible. The electron emission which leads to arc initiation was determined to be enhanced field electron emission (EFEE) by Cho and Hastings³. They described this current density from a finite emission site on the conductor surface as

$$j_{ec}(y) = A \frac{S_{FN}}{S_{real}} \beta^2 E^2 \exp\left(-\frac{B}{\beta E}\right), \quad (12)$$

which is the Fowler-Nordheim expression for field emission due to a thin dielectric layer with the added factor S_{FN}/S_{real} to account for the negative space charge effect near the emission site. The electric field E in this expression is the electric field at the dielectric-vacuum interface. A and B are the Fowler-Nordheim emission coefficients given by Eq. (8) and (9). The field enhancement factor β is assigned to the emission site to represent an enhancement

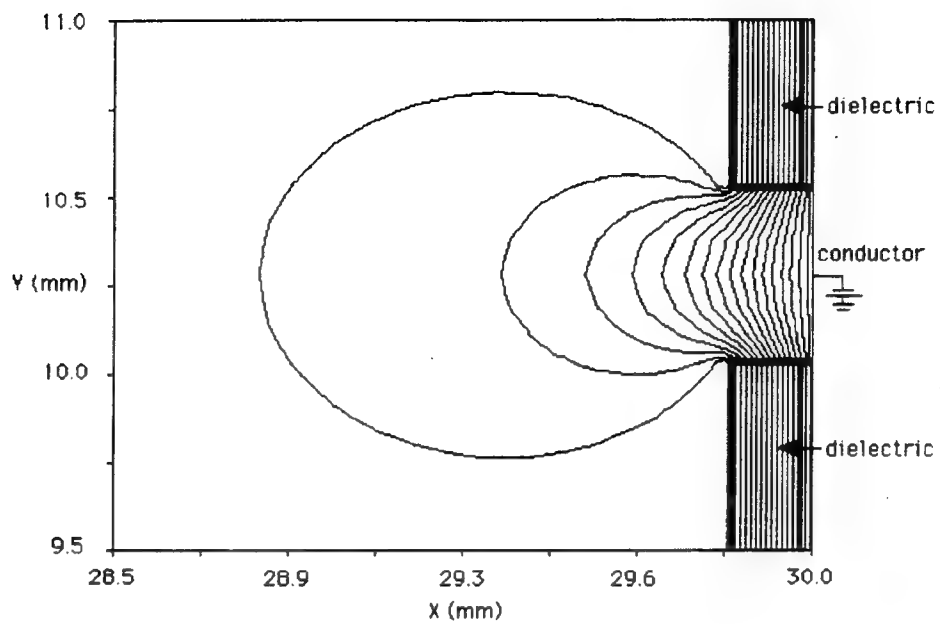


Figure 6: Typical electric potential contour plot for ambient ion charging of conventional cells

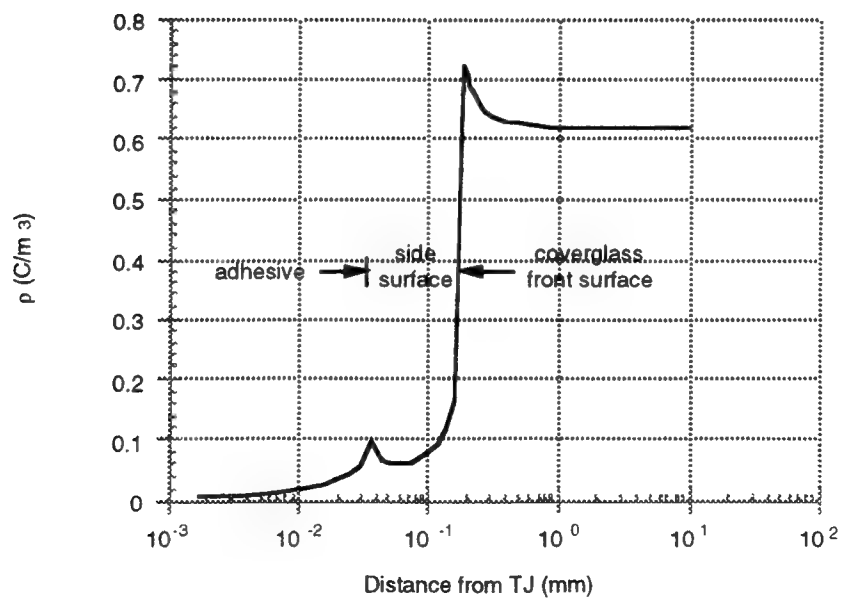


Figure 7: Typical surface charge density along side dielectrics after ambient ion charging of conventional cells

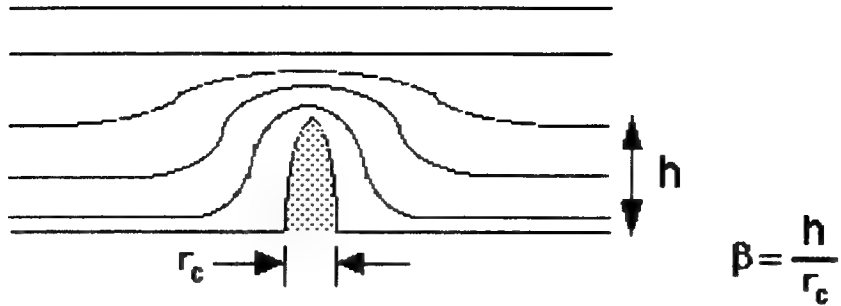


Figure 8: Electric field lines over a whisker on conductor surface

due to manufacturing defects or impurities. As shown in Figure 8, the protrusion causes a higher electric field gradient which enhances the electric field at its tip. From electrostatic theory for a whisker, β is the factor of the enhanced electric field at the tip of the whisker defect relative to the average electric field in the vicinity is equivalent to the ratio of the height of the protrusion to its radius of curvature. This factor can be of the order of 1 to 10^3 , with typical values of interest in the hundreds. The secondary electron current density at each point x is given by

$$j_{ee}(x, t) = \int \gamma_{ee}(x, y) P(x, y, t) j_{ec}(y, t) dy + \int \gamma_{ee}(x, x') P(x, x', t) j_{ee}(x') dx'. \quad (13)$$

In the orbit integration scheme, the first term in Eq. (11) is neglected since it was shown to be insignificant during electron charging³. Using Eq. (13), the surface charge density equation can be rewritten as

$$\frac{d\sigma(x, t)}{dt} = \int (\gamma_{ee}(x, y) - 1) P(x, y, t) j_{ec}(y, t) dy + \int (\gamma_{ee}(x, x') - 1) P(x, x', t) j_{ee}(x') dx'. \quad (14)$$

The orbit integration scheme then consists of

- (1) obtaining the surface potential by using the capacitance matrix method;
- (2) solving Laplace's equation to obtain the space potential;
- (3) integrating test electron orbits from the conductor to calculate γ_{ee} and the impact probabilities P for a given electron current density from the conductor;
- (4) solving Eq. (11) and (13) for the secondary electron current density j_{ee} and the rate of change of the surface charge density;
- (5) renewing the surface charge density;
- (6) obtaining the new potential for the renewed surface charge density;
- (7) calculating the timestep;
- (8) determining if the space charge current density is too high or the timestep is too small, either of which will halt the program; and

(9) calculating electron trajectories.

Steps (4) through (9) are repeated until the specified number of timesteps are completed or the program is stopped in step (8). If the space charge current density is too high, the space charge effects of the emission current can no longer be neglected so the PIC code must be run if further calculations are needed. If the timestep is too small, the electric field is most likely running away.

The timestep for EFEE charging is calculated based on the rate of change of the dielectric surface charge density at the first impact point $x = d_i$. This can be expressed by neglecting the second term in Eq. (11), reducing the equation to

$$\int_0^{d_i} \frac{d\sigma}{dt} dx = \int \left(\int_0^{d_i} P(x, y, t) dx \right) (\gamma_{ee} - 1) j_{ec}(y, t) dy. \quad (15)$$

The integral $\int_0^{d_i} P(x, y, t) dx$ is approximately unity since the point $x = d_i$ is the first impact point by emitted electrons. The equation then simplifies to

$$\frac{d\sigma}{dt} d_i = (\gamma_{ee} - 1) j_{ec}(y, t) \sqrt{S}. \quad (16)$$

or

$$\Delta t = \frac{\Delta\sigma}{(\gamma_{ee} - 1) j_{ec}(y, t) (\sqrt{S}/d_i)}, \quad (17)$$

where S is the area of the emission site, as shown in Figure 9. The potential difference between the triple junction ($x = 0$) and the impact point ($x = d_i$) can be expressed as

$$\phi_d = \frac{\sigma}{C_{diele}}, \quad (18)$$

where C_{diele} is the capacitance of the dielectric surface and σ is the surface charge density. The electric field, then, is approximately

$$E = \frac{\sigma}{C_{diele} d_i}. \quad (19)$$

The timestep can, therefore, be determined by solving

$$\Delta t = 0.02 \frac{\Delta E C_{diele} d_i}{(\gamma_{ee} - 1) j_{ec}(y, t) (\sqrt{S}/d_i)}, \quad (20)$$

where the empirical factor 0.02 is used so that the timesteps will be shorter than the actual timescale of arc initiation.

2.1.2 Analytical Model

The analytical model, which is used to calculate the arc rates, is drawn from the theory of Cho and Hastings^{3,9}, discussed in Section 1.2. The arc rate is determined by calculating the

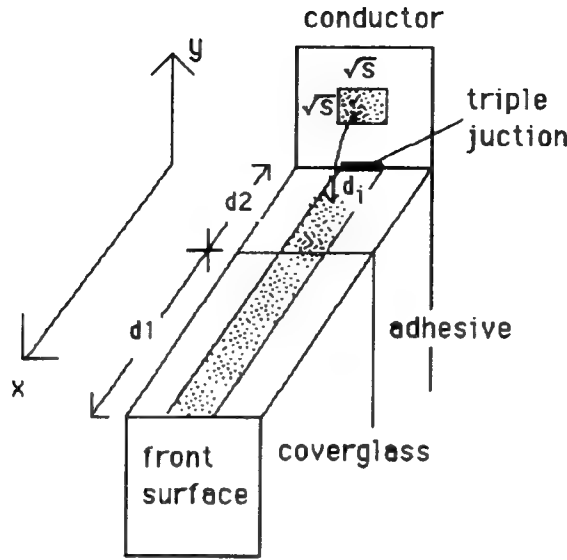


Figure 9: Geometry for EFEE charging

time between arcs, τ_{arc} , given by

$$\tau_{arc} = \min(\tau_{ion} + \tau_{efee}), \quad (21)$$

where τ_{ion} is the ambient ion charging time given by Eq. (6) and τ_{efee} is the enhanced field electron emission charging time given by Eq. (7). The analytical expression for τ_{efee} is determined by starting with Eq. (16). A schematic of the geometry considered is shown in Figure 9.

The electric field at the triple junction can be expressed as

$$E_{TJ} = \xi \frac{\phi_d}{d_i} = \xi \frac{\sigma}{C_{diele} d_i}, \quad (22)$$

where ξ is given by Eq. (10) if the first impact site of the electrons emitted from the interconnector is on the coverglass side surface. If it is on the adhesive side surface, ξ is unity. The electric field at the emission site, E_e , can be very different from the electric field at the triple junction. To account for this, the factor η is introduced so that

$$E_e = \eta E_{TJ} = \eta \xi \frac{\sigma}{C_{diele} d_i}. \quad (23)$$

Substituting Eq. (12) and (23) into Eq. (16) results in

$$\frac{dE_e}{dt} = \eta \xi \frac{(\gamma_{ee} - 1) \sqrt{S_{real}}}{C_{diele} d_i^2} A' \beta^2 E_e^2 \exp\left(-\frac{B}{\beta E_e}\right). \quad (24)$$

This can be integrated, assuming the secondary electron yield is constant, to obtain

$$E_e(t) = \frac{E_{e_0}}{1 + \frac{\beta E_{e_0}}{B} \ln \left(1 - \exp\left(-\frac{B}{\beta E_{e_0}}\right) \left(\frac{B}{\beta} \right) C t \right)}, \quad (25)$$

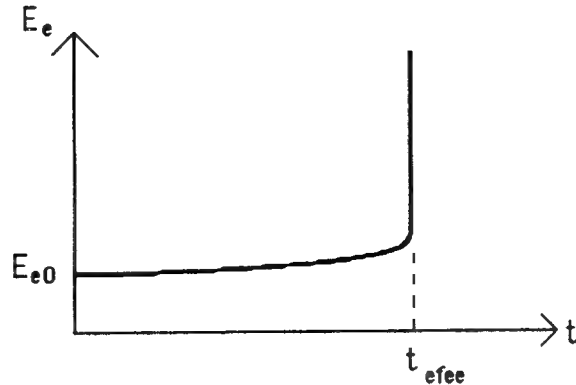


Figure 10: Typical electric field run-away versus time

where C is the constant given by

$$C = \eta \xi \frac{(\gamma_{ee} - 1) \sqrt{S_{real}}}{C_{diele} d_i^2} A' \beta^2 \quad (26)$$

and E_{e0} is the initial electric field at the electron emission site on the interconnector. From the numerical simulations it is known that the electric field E_e usually exhibits the behavior shown in Figure 10. The field run-away to infinity corresponds to the denominator of Eq. (25) reaching zero. This run-away time also corresponds to the time τ_{efee} , so τ_{efee} can now be determined:

$$\tau_{efee} = \frac{1 - \exp(-\frac{B}{\beta E_{e0}})}{\exp(-\frac{B}{\beta E_{e0}})} \left(\frac{B}{\beta} \right) C \quad (27)$$

$$\simeq \frac{\beta}{B} \exp\left(\frac{B}{\beta E_{e0}}\right) \frac{1}{C} \quad (28)$$

$$= \frac{C_{diele} d_i^2}{(\gamma_{ee} - 1) \sqrt{S_{real}} \eta \xi A \frac{S_{EN}}{S_{real}} B \beta} \exp\left(\frac{B}{\beta E_{e0}}\right). \quad (29)$$

This equation is the same as Eq. (7) with E_{e0} expressed as the potential difference between the coverglass front surface and the triple junction:

$$E_{e0} = \eta \frac{V}{d} \xi_0. \quad (30)$$

Finding the minimum of the sum of the ion and EFEE charging times accounts for the fact that EFEE charging can initiate whenever the surface has a strong enough electric field, not just when the front surface current returns to zero. To find this minimum charging time, electron emission sites must be considered along the entire conductor as opposed to the numerical model which sets one emission site usually next to the triple junction. For each emission site a voltage V_e can be calculated at which the arc occurred by solving the differential equation

$$\frac{d\tau_{arc}}{dV_e} = 0, \quad (31)$$

or

$$\frac{d}{dV_e} \left[\frac{(V_e - (V_{arc} - \frac{\Delta Q}{C_{front}}))C_{front}}{en_e v_{ion} A_{cell}} + \frac{C_{diele} d_i^2}{(\gamma_{ee} - 1)\sqrt{S_{real}}\eta\xi A \frac{S_{EN}}{S_{real}} B \beta} \exp\left(\frac{Bd}{\beta V_e \eta \xi_0}\right) \right] = 0. \quad (32)$$

where V_{arc} is the voltage of the last arc discharge and C_{front} is the capacitance of the coverglass front surface.

In order to solve Eq. (32), a number of properties must be known or determined. First, the following cell properties must be known: the thickness of the coverglass and cover adhesive (d_1, d_2), the dielectric constants of the coverglass and adhesive ($\epsilon_{d_1}, \epsilon_{d_2}$), the energy of incident electrons for maximum secondary electron yield for the coverglass and adhesive (E_{max_1}, E_{max_2}), the maximum secondary electron yield at normal incidence for the adhesive and coverglass ($\gamma_{max_1}, \gamma_{max_2}$), the interconnector work function (ϕ_w), and the solar cell frontal area (A_{cell}). Then, the following factors can be determined: A according to Eq. (8); B from Eq. (9); ξ and ξ_0 from Eq. (10); $d = d_1 + d_2$; C_{front} which is approximated as

$$C_{front} = \frac{1}{(A_{cell}\epsilon_{d_1})/d_1 + (A_{cell}\epsilon_{d_2})/d_2}; \quad (33)$$

and γ_{ee} which is given by Reference 8

$$\gamma_{ee} = \gamma_{max} \frac{E_i}{E_{max}} \exp\left(2 - 2\sqrt{\frac{E_i}{E_{max}}}\right) \exp[2(1 - \cos \theta_i)]. \quad (34)$$

Here, E_i is the incident energy of the emitted electrons impacting the dielectrics given by

$$E_i = e\phi_d = \frac{E_{TJ}d_i}{\xi} = \frac{\xi_0}{\xi} V \frac{d_i}{d} \quad (35)$$

and θ_i is the incident angle of those electrons at the first impact site given by

$$\theta_i = \arctan\left(\frac{d_i}{y}\right), \quad (36)$$

where y is the distance of the emission site from the triple junction. The mission parameters determine the ion velocity v_{ion} and the range of the ambient density n_e . If the array is orientated at 90° to the ram velocity, v_{ion} is the orbital velocity. Otherwise, v_{ion} is a sum of the orbital velocity and the mean thermal speed of ions $\bar{c}_i/4$, where

$$\bar{c}_i = \sqrt{\frac{8T_i}{\pi m_i}}. \quad (37)$$

Consequently, the ion mass and electron temperature must also be known. For each arc calculation, n_e is chosen randomly from a uniform distribution in $\log_{10} n_e$. Other properties only known within a range include areas S_{eff} and S_{real} and enhancement factor β . Areas

S_{eff} and S_{real} are randomly chosen from uniform distributions in $\log_{10} S_{eff}$ and $\log_{10} S_{real}$, respectively, between given minimum and maximum values. The enhancement factor β is randomly selected from the distribution $f(\beta) = f_o \exp(-\beta/\beta_o)$, where f_o is determined from the normalization: $\int f(\beta) d\beta = 1$. Finally, the three parameters left to be determined are C_{diele} , d_i , and η , all of which are functions only of the emission site distance y from the triple junction. To determine C_{diele} , the capacitance matrix scheme used with unit surface charge values must be run. The relevant values are the diagonal elements. Those that correspond to the lower side dielectric are non-dimensionalized by the normal capacitance

$$C_{norm} = \frac{1}{\frac{d_1}{\epsilon_{d_1}} + \frac{d_2}{\epsilon_{d_2}}} \quad (38)$$

and inverted. The corresponding distances from the triple junction are non-dimensionalized by the thickness of the two dielectrics, d . These values are plotted and fit to a five order polynomial:

$$C_{diele}^{-1} = \sum_{n=0}^{n=5} c_n \left(\frac{d_i}{d} \right)^{n-1}. \quad (39)$$

To determine d_i and η , results from the orbit integration scheme of the numerical model are used to obtain functional forms. These are

$$\frac{d_i}{d} = \sum_{n=1}^{n=4} b_n \left(\frac{y}{d} \right)^{\frac{1}{2n}} \quad (40)$$

and

$$\eta = \frac{E_e}{E_{TJ}} \sum_{n=1}^{n=4} a_n ((\bar{y} - 1)^{2n} - 1), \quad (41)$$

where $\bar{y} = y/(d_{gap}/2)$.

The voltage V_e is determined to be in the range of V_i , the voltage differential between the front surface and conductor just after the arc, and V_{bias} . If τ_{effee} dominates to the point where τ_{ion} is insignificant, $V_e = V_i$. Likewise, if τ_{ion} dominates, $V_e = V_{bias}$. Otherwise, the arcing time is affected by both τ_{effee} and τ_{ion} , so V_e is determined by the Newton-Raphson method. After τ_{arc} is calculated for every emission site, typically numbering 1000, the smallest τ_{arc} is compared with the experiment time, τ_{exp} . If τ_{exp} is greater than τ_{arc} , another τ_{arc} is calculated until the sum of the arcing times is greater than τ_{exp} . The arc rate is then the number of arcs counted less one divided by the experiment time.

For a given solar array, the surface is divided into sections of area equivalent to the area covered by the arc discharge wave. Based on experimental measurements in Reference 9, this area is chosen to be 0.012m^2 . All arcs in a section are assumed to be correlated, but arcs are assumed to be uncorrelated between different sections. The arc rate is calculated

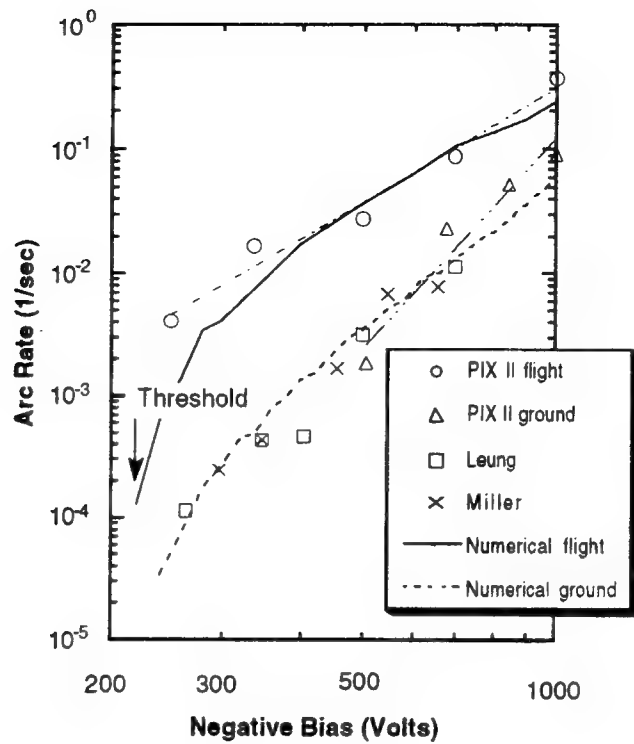


Figure 11: Experimental data for ground and flight experiments

for each correlated area independent of the other areas. If there is more than one correlated area, the actual arc rate for the array is the sum of the arc rates of each area.

Cho and Hastings use this procedure in Reference 3 to calculate the arc rate numerically for the PIX II flight and ground experiments. As can be seen in Figure 11, the results show excellent agreement with the data over the range that the data exists. They predict a threshold when the charging process is exponentially slow and also predict a saturation for high voltages. The lower parts of the curves cover the regime where the enhanced field electron emission charging is the slowest charging process in the system. The arc rate dependence on voltage here is exponential and enables a threshold voltage to be defined with a small uncertainty. This threshold voltage can be defined as the voltage at which the arc rate is decaying very rapidly. The upper parts of the arc rate curves cover the regime dominated by the ion recharging time. This leads to a decrease in the rate of change of arc frequency as can be clearly seen in the data. The fact that the arc rate scales with the density for the higher voltages can also be explained from the dominance of the ion recharging time since this scales directly with density.

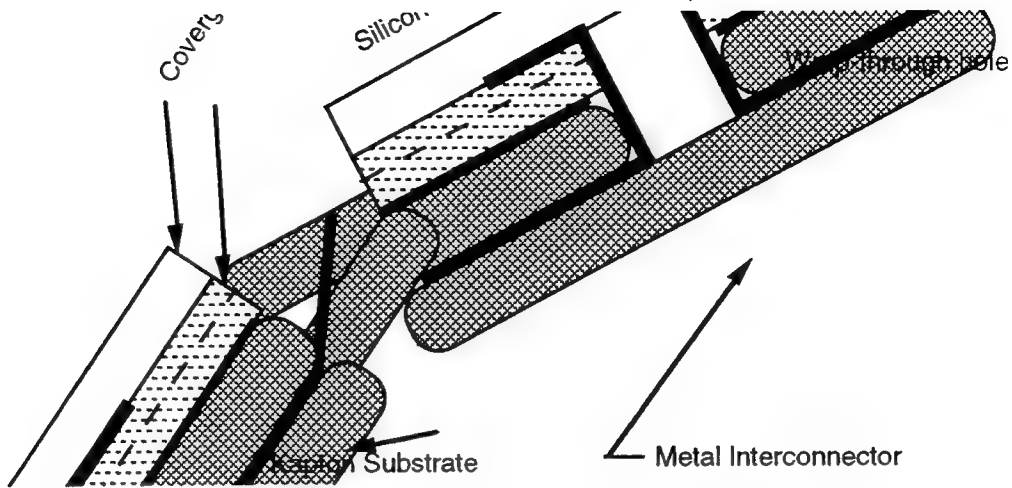


Figure 12: Schematic of a wrap-through-contact solar array

2.2 Wrap-Through-Contact Cells

A schematic of a wrap-through-contact (WTC) solar cell is shown in Figure 12. Kapton covers the metal interconnector so it is not exposed to the ambient plasma environment like the interconnectors of conventional cells. One of the reasons for this design was to eliminate arcing at the interconnector-cell interface. On the edge of the cell, however, the semiconductor cell itself is exposed. Since the semiconductor is adjacent to both a dielectric coverglass and a dielectric substrate, arcing can occur. In ground tests, arcing occurred on WTC cells at bias voltages as low as -400V. Consequently, a model is needed to understand how arcing occurs on this type of cell.

As with the conventional cell, the area of interest for studying electric field buildup can be simplified to two dielectrics and a conductor. In this case, the conductor is situated between the two dielectrics as shown in Figure 13. The numerical model for the conventional cells could be modified by a simple change of boundary conditions. The problem is more complex, however, as the conductor is now in the computational domain instead of being merely a boundary condition. In addition, the lower dielectric can not be treated as a simple boundary as the conductor was in the conventional cell model. To properly include the dielectric properties of the substrate, a dielectric of two grid cells thickness is added beneath the conductors and in the gap between the cells. The new geometry also has two triple junctions on each of the two conductor edges, making the previous grid clustering inadequate. The grid is, therefore, altered to again cluster near the triple junctions as well as along the side surfaces, as shown in Figure 14.

In Section 2.1.1 the results of the ambient ion charging calculated by the PIC scheme

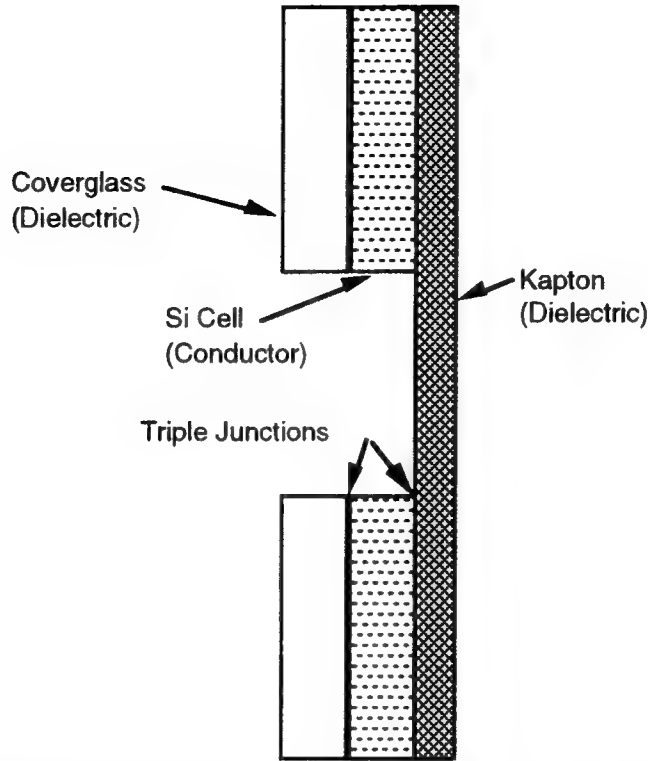


Figure 13: Wrap-through-contact solar array model used for numerical simulations

are represented by the electric potential plot (Figure 6) and the surface charge density plot (Figure 7). Corresponding plots for the WTC geometry are shown in Figures 15 and 16. As expected, the highest potential value is on the conductor surface with gradients falling off quickly around this voltage source. The gap is sufficiently large that the gradients do not interfere but rather connect at the coverglass surface. The potential lines fall off uniformly beyond the coverglass surface. Above the substrate surface, the potential gradients concentrate near the conductor with potential lines peaking sharply in the center due to the grid configuration. In the coverglass, the potential gradients are curved near the edge of the cell but straighten away from the cell edge.

To simulate the electric field build up, the modified PIC code is run with the enhanced electron field emission (EFEE) charging processes included. The initial conditions are obtained from the results of the ambient ion charging calculations and the enhancement factor, β , for each conductor cell. Due to the high electric potential normal to the conductor surface, much lower enhancement factors ($\beta \approx 30\text{-}60$) are used to reduce the number of electrons emitted from the conductor. When too many electrons are emitted, the EFEE charging time is too small, making it less than or on the order of a capacitor charging time. The timestep also affects the number of particles injected into the domain, so it is typically

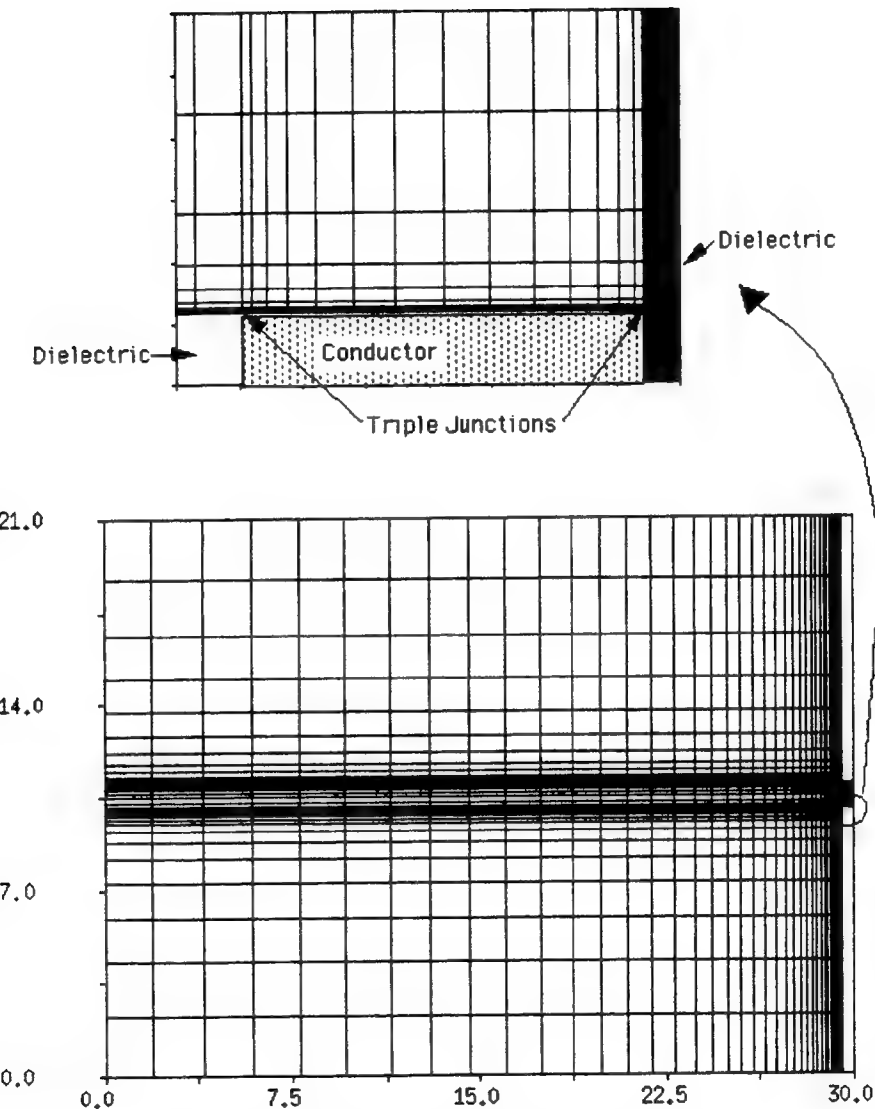


Figure 14: Typical grid structure for calculations

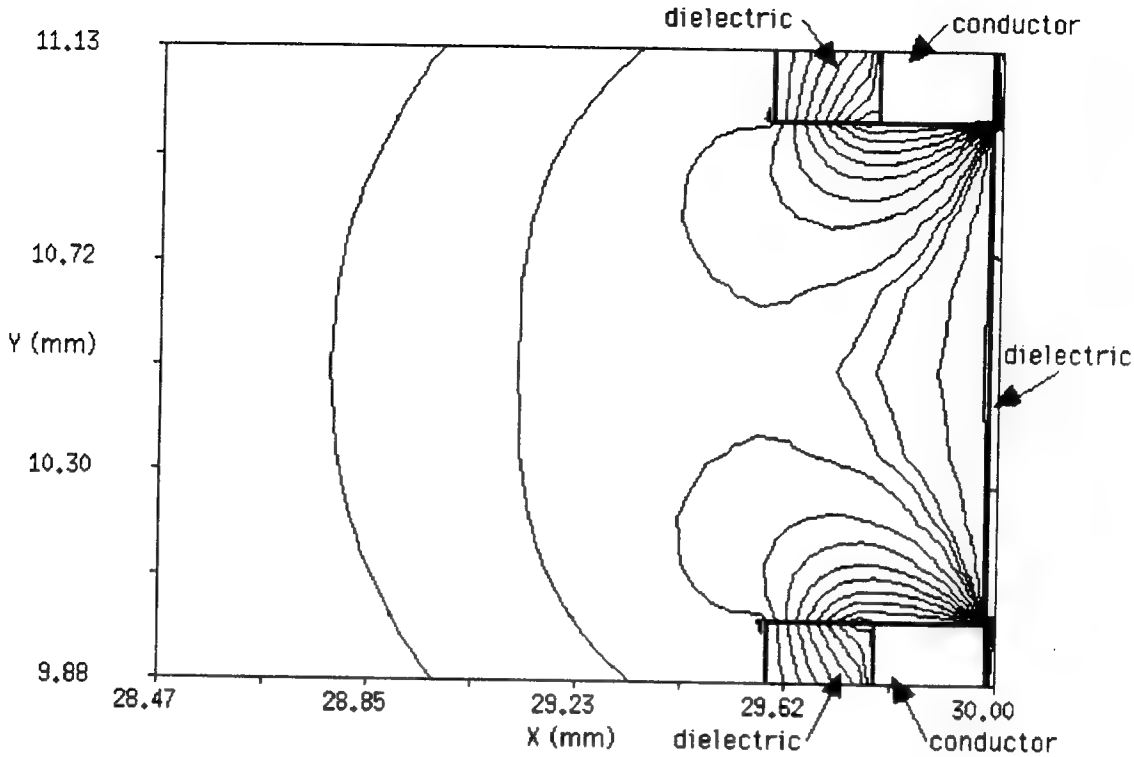


Figure 15: Typical electric potential for ambient ion charging of WTC cells

chosen to be $\omega_{pe}\Delta t = 0.01$. Larger timesteps can be used when fewer particles are in the domain, which occurs when the electric field at the triple junction has not increased enough for EFEE charging to begin. The PIC code is run until the electric field runs away at one or both of the triple junctions. Since the PIC code automatically accounts for space charge effects, the simulation is often run beyond the electric field runaway into the space charge current limited regime, which limits the electric field magnitude.

The cell properties used for the WTC simulations are based on the Space Station Freedom WTC cell. The coverglass and semiconductor are each $203\mu\text{m}$ (8 mil) thick, and the cell gap is 1mm. The semiconductor is silicon, which has a work function of 4.85eV. The coverglass is assumed to be ceria-doped microsheet (CMX) with a dielectric constant of 4 and secondary electron properties of $E_{max} = 400\text{V}$ and $\gamma_{max} = 4$. The Kapton substrate has a dielectric constant of 3.5 and assumed secondary electron properties of $E_{max} = 300\text{V}$ and $\gamma_{max} = 3$.

The EFEE charging of the WTC cells over the range of 300-500V is distinguished by two classes of behavior, the first occurring with lower β values (~ 30) and the second occurring with higher β values ($\sim 50-60$). As seen in Figures 17 and 18, the electric field at the upper triple junction increases initially for the first class and decreases initially for the second

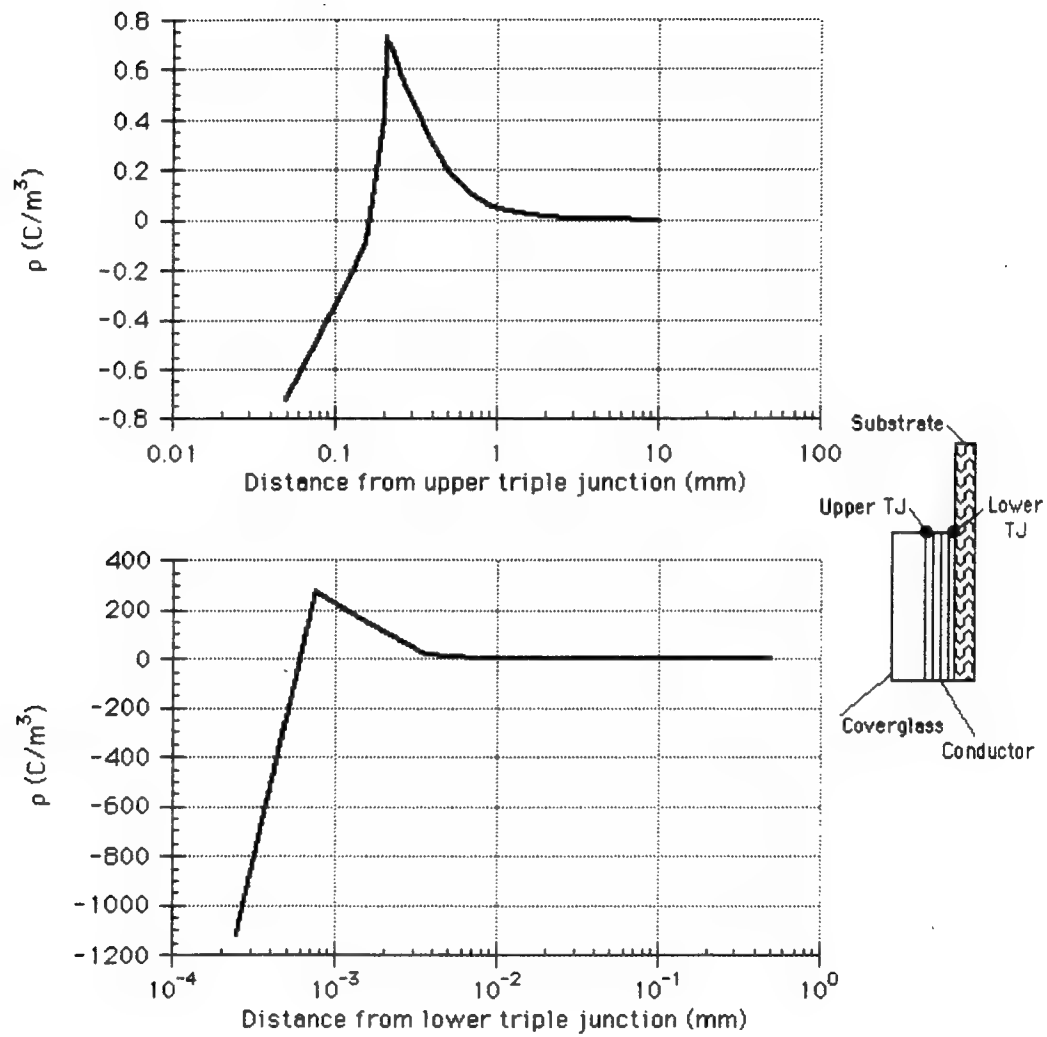


Figure 16: Typical surface charge density along the side dielectric surface after ambient ion charging of WTC cells

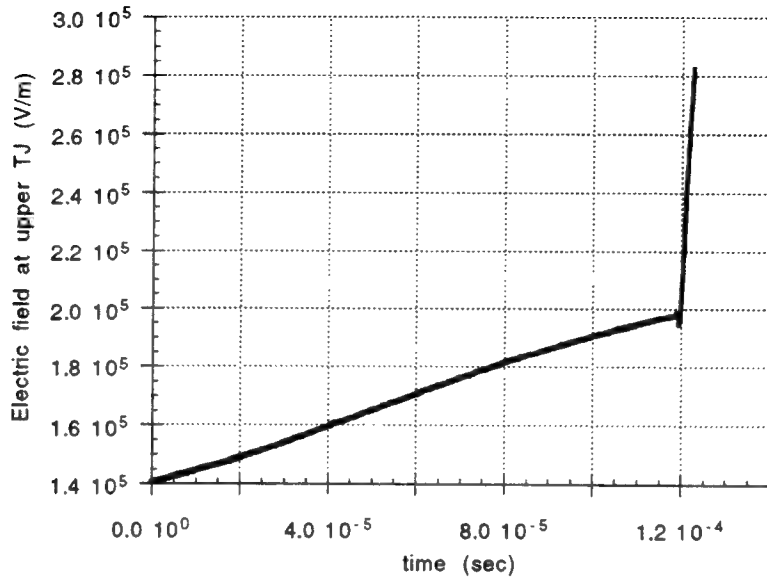


Figure 17: Class 1 electric field at upper triple junction versus time

class. No runaway occurs at the lower triple junction within this time.

In the first class, the ambient ion charging continues to build up the electric field at the upper triple junction until it is high enough to initiate EFEE charging. Once initiated, the high flux of electrons causes the field to decrease for a short time before the runaway. As shown in Figure 19, the surface charge along the side of the coverglass does not change much during the ambient ion charging, as expected, but also does not change much during the electric field runaway. The surface charge along the front surface, however, does increase substantially, indicating that the electrons from the conductor are striking there and increasing the surface charge through secondary electron emission.

In the second class of behavior EFEE charging begins immediately, emitting many electrons into the domain. Although the surface charge density does increase, as shown in Figure 20, most of the electrons quickly exit the domain without striking any of the cell surfaces. Just prior to runaway, the difference between the number of electrons emitted and the number of electrons impacting the dielectric increases substantially at the same time that the total number of electrons in the domain increases substantially. The electric field then runs away, and the surface charge density along the coverglass side and front surfaces increases significantly.

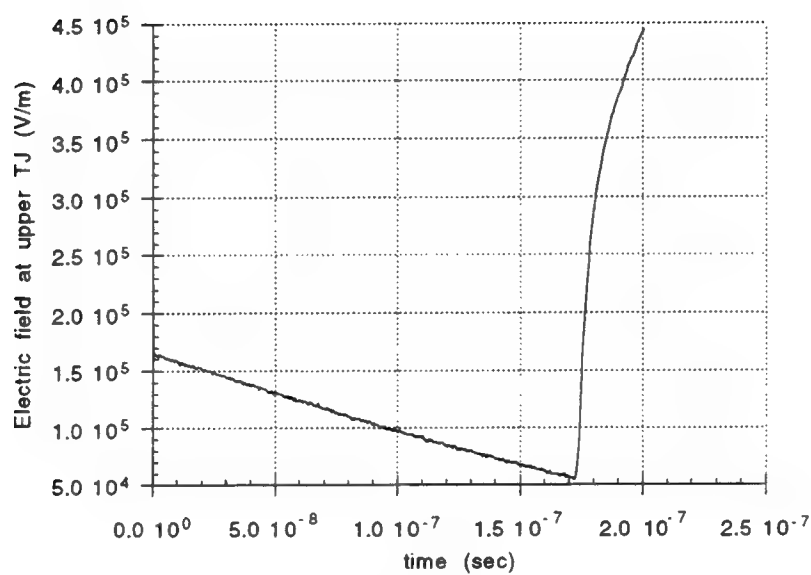
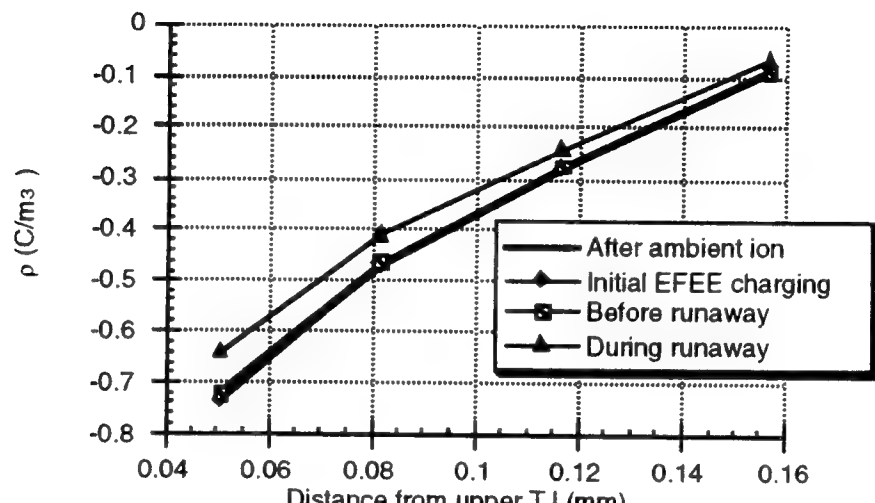
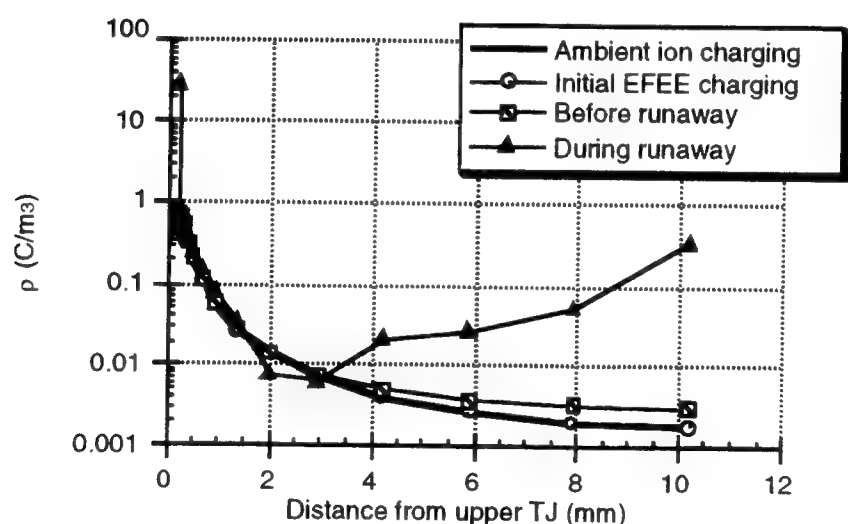


Figure 18: Class 2 electric field at upper triple junction versus time



(a) Coverglass side surface



(b) Coverglass front surface

Figure 19: Class 1 surface charge density over the coverglass (a) side surface, (b) front surface

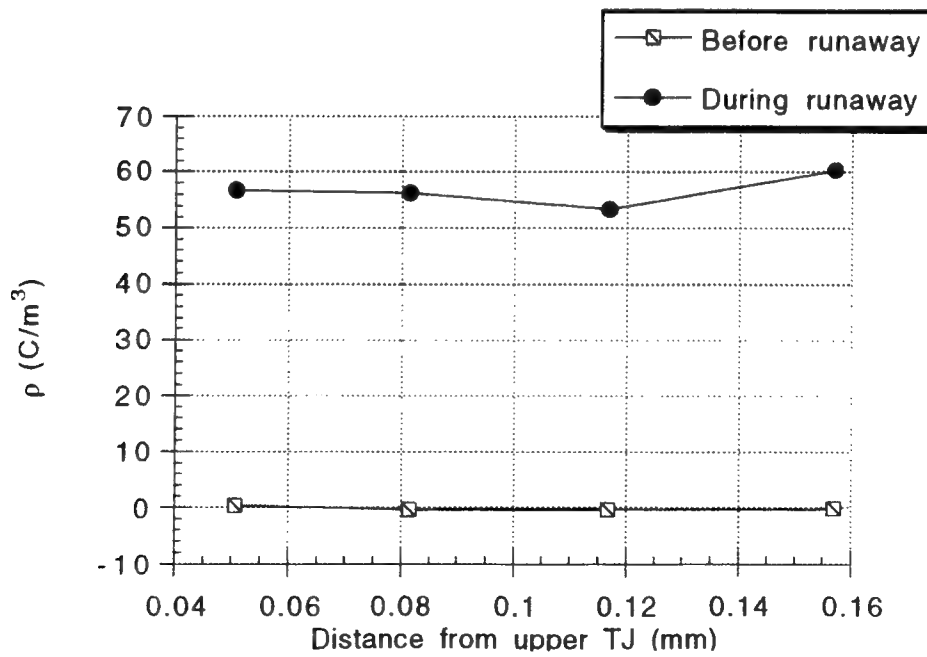
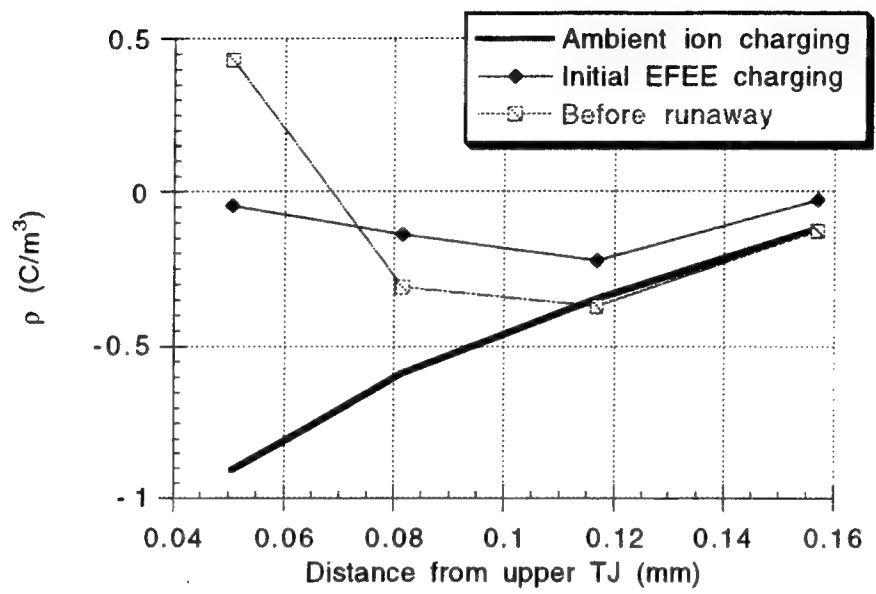


Figure 20: Class 2 surface charge density over the coverglass side surface

Chapter 3

Arc Mitigation Methods

In this research several methods of reducing the arc rate were studied. As expressed in Eq. (5), the arc rate is the inverse of the sum of the two charging times, the ambient ion charging time τ_{ion} and the enhanced electron field emission (EFEE) charging time $\tau_{e_{fee}}$. Since τ_{ion} is dependent mainly on mission parameters such as the ambient plasma density, arc rate mitigation can only be achieved by increasing $\tau_{e_{fee}}$, which is affected by cell properties only. From Eq. (7), the properties which affect $\tau_{e_{fee}}$ to the greatest extent are those in the exponential factor and the secondary electron yield γ_{ee} , which causes the time to be non-existent if it is equal to or less than unity. In addition, lengthening the coverglass over the interconnector to obstruct the electron trajectories should also increase $\tau_{e_{fee}}$, if only by increasing the distance over which the surface charge must build up.

For all numerical simulations described in this chapter, the domain size used is 3mm in the x direction and 2.5mm in the y direction, which includes one-half of two 2mm wide cells and a 0.5mm gap in between them, as shown in Figure 5. The simulations assumed the same environment of $n_e = 5 \times 10^{11} \text{ m}^{-3}$, $T_i = T_e = 0.1 \text{ eV}$, and a kinetic energy of incoming ions of 5eV, all typical of low earth orbit. A 90° orientation to the ram velocity was used for simplicity. In addition, the emission site on the conductor was set adjacent to the triple junction with an area of $S_{real} = 1.2 \times 10^{-13} \text{ m}^2$, as determined by the grid cell length at that location. Since EFEE charging is dependent on an emission site near the triple junction, this condition should define the upper bound for $\tau_{e_{fee}}$.

3.1 Control Case

The cell used as the control case for these arc rate simulations is the silicon conventional cell without a coverglass overhang. The input parameters chosen to simulate this cell are shown in Table 1. The dielectrics are a fused silica coverglass and DC 93500 adhesive, and the interconnector material is Kovar. The interconnector work function is taken to be the

Table 1: Conventional silicon cell data used in numerical simulations

d_1	0.153mm
d_2	0.037mm
ϵ_{d_1}	3.5
ϵ_{d_2}	2.7
γ_{max1}	3.46
γ_{max2}	3.0
E_{max1}	330V
E_{max2}	300V
d_{gap}	0.5mm
ϕ_w	4.76eV

weighted average of the work functions of the elements which compose it. The dielectric thicknesses are typical values.

To determine the effect of varying each parameter, two calculations are made. First, the numerical code discussed in Section 2.1.1 is used to determine τ_{effee} over a range of typically 5 values of βV . The charging time τ_{effee} is then plotted against βV since the analytic theory⁹ indicates that τ_{effee} is a strong function of βV . This plot is shown in Figure 21 for the control case over a relevant range. Times less than 1×10^{-8} sec are not useful as that interval is on the order of a capacitor build-up time. Times greater than 1×10^4 sec are also not useful as either the ion charging time would dominate or the orbit would be completed, causing the power system to regenerate. In the following property variations, however, the same range of βV is maintained where possible to simplify comparisons.

Second, the analytical model discussed in Section 2.1.2 is used to determine the arc rates. In this model, the arcing time is determined by the one emission site on a conductor of typically 1000 sites that has the shortest charging time of all the cells. This is a more realistic simulation than the numerical simulations in which only the effect of one site on one conductor was studied. Hence, the effects determined by the numerical simulations often do not have as much impact on the arc rate results as one might expect. The experiment time is also a consideration, particularly for lower voltages where arcing takes a longer time to occur. For the control case and the mitigation cases the experiment time is arbitrarily chosen to be one second. Also, arc rates are calculated at intervals of -100V. The arcing rates for the control case are shown in Figure 22. The curve clearly shows the two dominating regions of

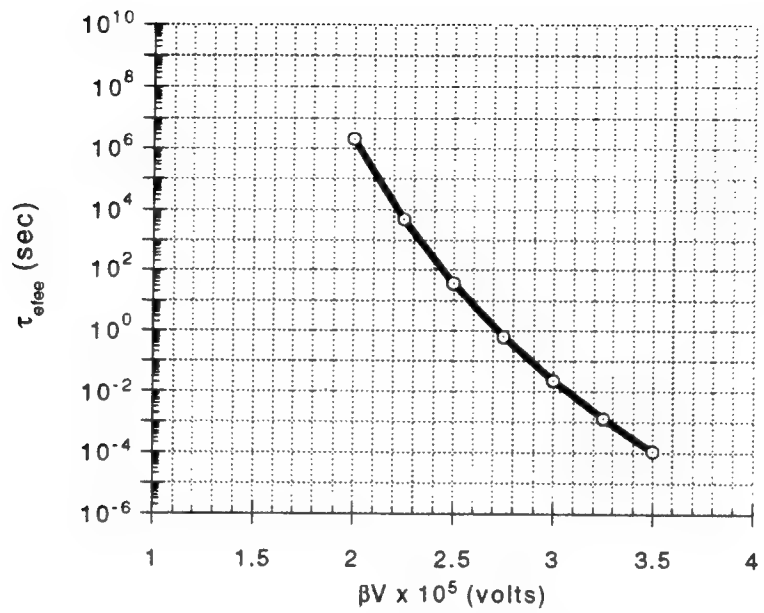


Figure 21: Enhanced field electron emission charging time, τ_{efee} , versus βV for the silicon conventional control case

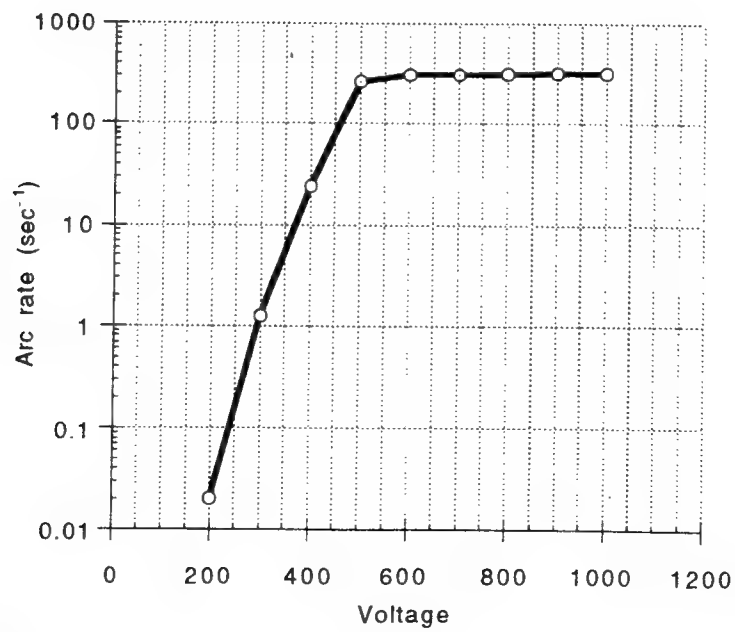


Figure 22: Analytic arc rates for the silicon conventional control case

$\tau_{e\text{fee}}$ and τ_{ion} . At lower voltages, $\tau_{e\text{fee}}$ dominates and the arc rate is a strong function of the voltage. At higher voltages, τ_{ion} limits the arcing rate to the value determined by mission parameters, which is a weak function of the voltage. Consequently, the arc rate mitigation methods studied are intended to shift and alter the slope of the $\tau_{e\text{fee}}$ dominated region. The τ_{ion} dominated region can also be shifted though it will remain at the same arc rate. The arc rate results are presented at the end of the chapter in a separate section so that comparisons may be made among all methods studied.

3.2 Interconnector Material

The work function of the electron emitting surface determines the ease with which electrons are released. If the number of electrons emitted from the interconnector is reduced, the time for the electric field at the triple junction to build up will be increased. In the analytical formula for $\tau_{e\text{fee}}$, the work function determines the value of the Fowler-Nordheim coefficients A and B given by Eq. (8) and (9). Figure 23 shows $\tau_{e\text{fee}}$ plotted against βV over a range of significant values for varying work functions. As expected metals with work functions higher than the control case of 4.76eV have longer times for EFEE charging, and metals with lower work functions have shorter times.

These numerical simulation results can easily be predicted from the theory. To determine the effect of a different work function ϕ_{w_2} , we can solve the ratio $\tau_{e\text{fee}}(\phi_{w_2})/\tau_{e\text{fee}}(\phi_w)$ using Eq. (7):

$$\frac{\tau_{e\text{fee}}(\phi_{w_2})}{\tau_{e\text{fee}}(\phi_w)} = \exp \left((\phi_{w_2}^{1.5} - \phi_w^{1.5}) \frac{6.53 \times 10^9 d}{\beta V \eta \xi_0} \right) \quad (42)$$

The only unknown variable is η , which is within the range 1.001-1.005 for emission sites adjacent to the triple junction. For the cases shown in Figure 23, this expression is evaluated and plotted with the equivalent numerical values in Figure 24. The predictions are all within the margin of error for the analytical and numerical values, except for the extreme case of $\phi_w = 5.9\text{eV}$ which is predicted about an order of magnitude too high. This is therefore a useful tool for predicting the effect of changing the exposed interconnector metal.

3.3 Dielectric Thickness

Another method of reducing the arc rate is to increase the dielectric thickness, $d = d_1 + d_2$. This increases the surface on which charge can accumulate and reduces the average charge density. The analytic theory⁹ accounts for changes in thickness in the exponential factor of $\tau_{e\text{fee}}$. The exponential factor also includes ξ , which is dependent on the ratio of dielectric

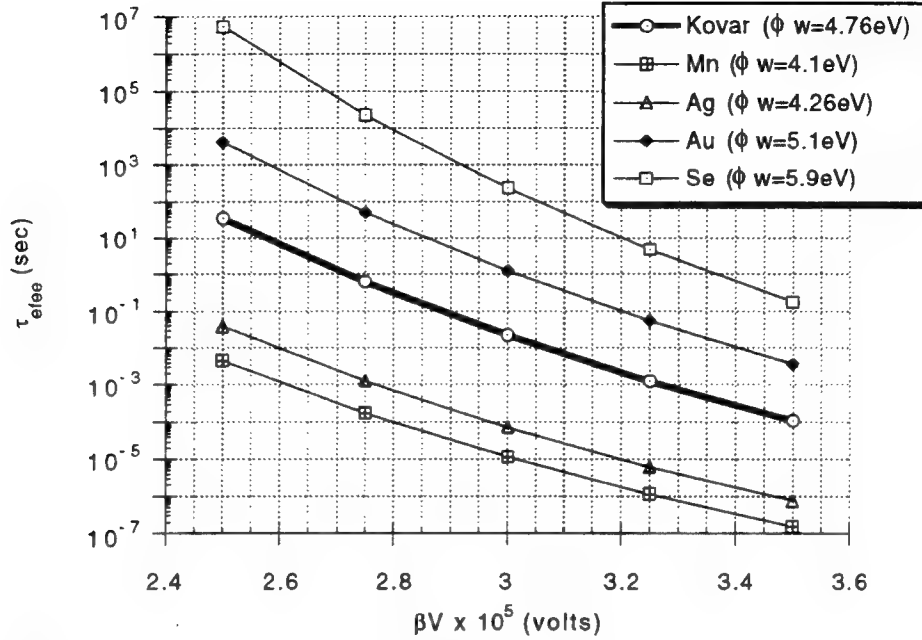


Figure 23: Enhanced field electron emission charging time, τ_{efee} , versus βV for different work functions, ϕ_w (eV)

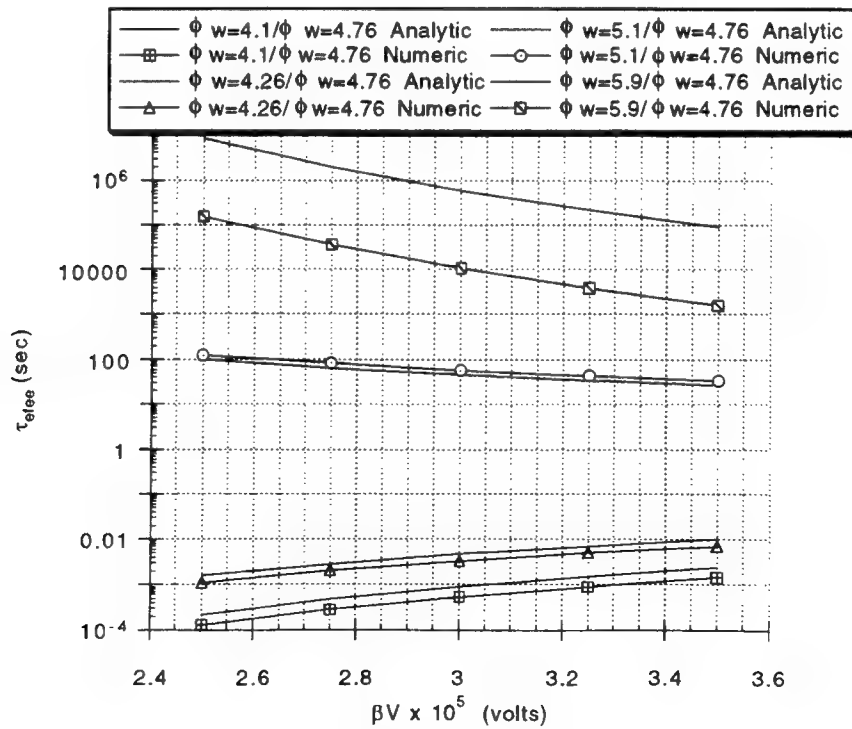


Figure 24: Analytic predictions and numerical results for $\tau_{efee}/\tau_{efee}(\phi_w = 4.76 eV)$ versus βV

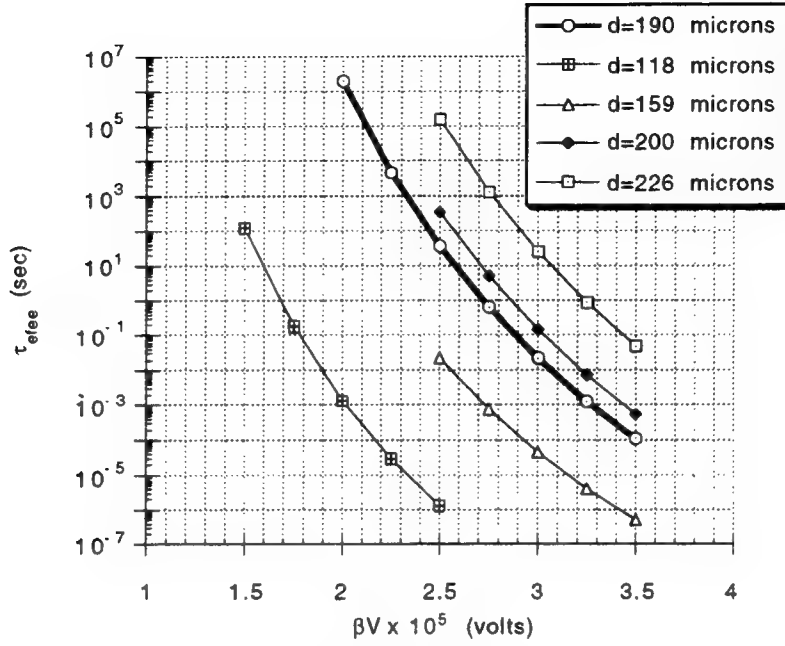


Figure 25: Enhanced field electron emission charging time, τ_{efee} , versus βV for different dielectric thicknesses, $d(\mu\text{m})$

thicknesses, d_1/d_2 . In order to exclude this factor, the ratio is the same for each case studied. Further simulations which studied the effect of this ratio showed that it did not alter the results. Figure 25 shows τ_{efee} plotted against βV for the control case and for four cases with differing thicknesses. As expected, increases in thickness increase τ_{efee} significantly.

By calculating the ratio of $\tau_{efee}(d + \Delta d)/\tau_{efee}(d)$ using Eq. (7), the change in τ_{efee} can again be easily predicted:

$$\frac{\tau_{efee}(d + \Delta d)}{\tau_{efee}(d)} = \exp \left[\left(\frac{d + \Delta d}{d} \right) \left(\frac{B}{\beta V \eta \xi_0} \right) \right] \quad (43)$$

The analytic results are plotted with the numerical results in Figure 26. The predictions are all within the accuracy of the numerical simulations. The prediction for the largest variation of $d = 118\mu\text{m}$ is only off by a factor of 3. Using the same control case, an increase in thickness to $250\mu\text{m}$ would result in an increase in τ_{efee} of nearly 6 orders of magnitude. This will effectively eliminate electric field run away. Meanwhile, a decrease in thickness to $50\mu\text{m}$ would result in a decrease in τ_{efee} of nearly 14 orders of magnitude. In this case the arcing rate will be dominated by the ion recharging time, τ_{ion} . These results indicate that the new thinner solar cells such as Advanced Photovoltaic Solar Array (APSA) will experience higher arcing rates at relatively low voltages.

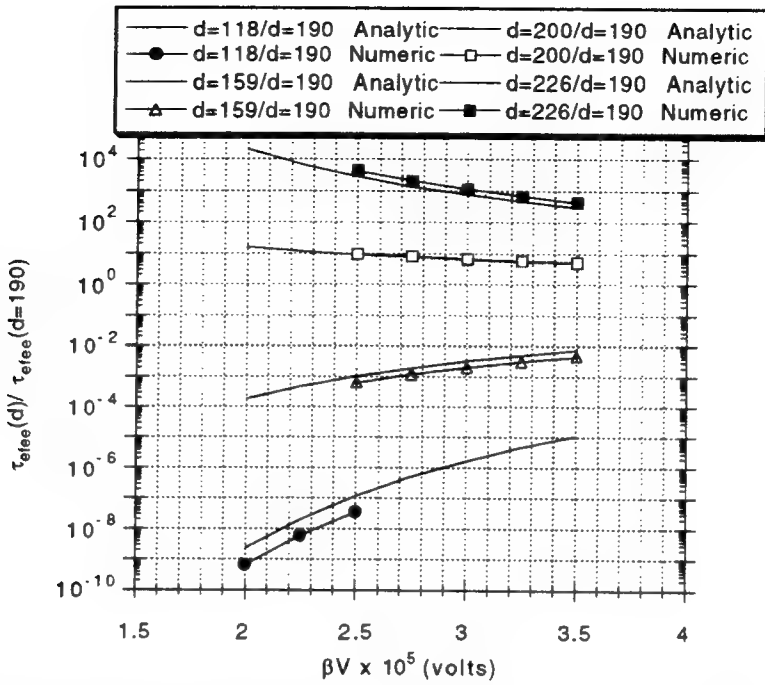


Figure 26: Analytic predictions and numerical results for $\tau_{efee}/\tau_{efee}(d = 190\mu m)$ versus βV

3.4 Secondary Electron Yield

The secondary electron yield, γ_{ee} , from the dielectrics must be greater than unity for the electric field to build up and run away. If γ_{ee} is equal to unity, the electric field will assume a steady state and no charge accumulation will occur. If γ_{ee} is less than unity, the electric field will decrease as negative charge accumulates on the dielectrics. This is modeled in Eq. (7) by the factor $(\gamma_{ee} - 1)^{-1}$.

A sensitivity scan of τ_{efee} over relevant values of βV for γ_{ee} values of actual materials is shown in Figure 27. As in the previous sensitivity scans, only the property of interest, γ_{ee} , is varied from the control case. In these cases, γ_{ee} is the same for both dielectrics, although the control case has slightly different values of γ_{ee} for the two dielectric materials, fused silica and DC 93500. In order to choose relevant values, the Eq. (34) for γ_{ee} is evaluated for different γ_{max} and E_{max} values determined for actual materials. Since the ambient ion charging is not calculated with secondary electron effects, the initial conditions for EFEE charging are the same as for the control case for every γ_{ee} variation. Consequently, d_i must only be known for the control case to determine γ_{ee} for any other set of secondary electron parameters. From the numerical simulation of the control case, d_i is $35.6\mu m$, so θ_i is estimated to be 89° , and E_i is estimated to be $75V$. For the control case the estimated γ_{ee} is 15, but the numerical results showed γ_{ee} to be 7. In the other cases studied the

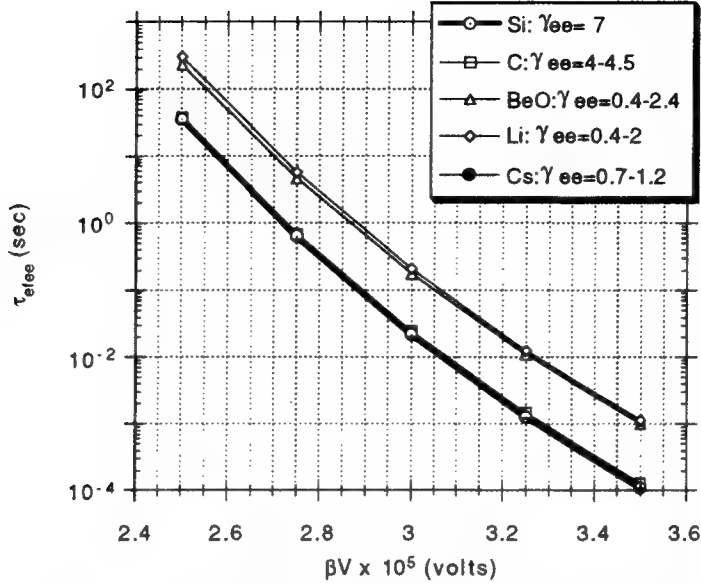


Figure 27: Enhanced field electron emission charging time, τ_{efee} , versus βV for different secondary electron yields, γ_{ee}

estimated values of γ_{ee} are also about a factor of 2 higher than the calculated values. The lowest estimated value studied is $\gamma_{ee} = 2.5$ for cesium's properties, but the calculated value is $\gamma_{ee} = 0.7-1.2$. The latter corresponds to the result of no electric field run away by the numerical simulation. The results are shown in Figure 27 with the numerical values of γ_{ee} . As expected, cases with secondary electron yields near unity have much longer EFEE charging times, and the case (Cs) with γ_{ee} values near and less than unity has an infinite EFEE charging time since the electric field at the triple junction did not run away.

One difference between the analytical and numerical results is the effect of the dielectric surface charge, which is not taken into account in the analytical model. As shown in Figure 28, the surface charge next to the triple junction is negative during EFEE charging for the Cs case of $\gamma_{ee} = 0.7-1.2$, causing the electric field to be unable to run away. In the Li case of $\gamma_{ee} = 0.4-2$, the surface charge builds up over time as it must for the electric field to build up. This surface charge density effect is discussed further in the next section.

3.5 Dielectric Constants

The effect of different dielectric constants is not as apparent in the analytical formula for τ_{efee} (Eq. (7)) as for the other cell properties. In the analytical formula, the dielectric

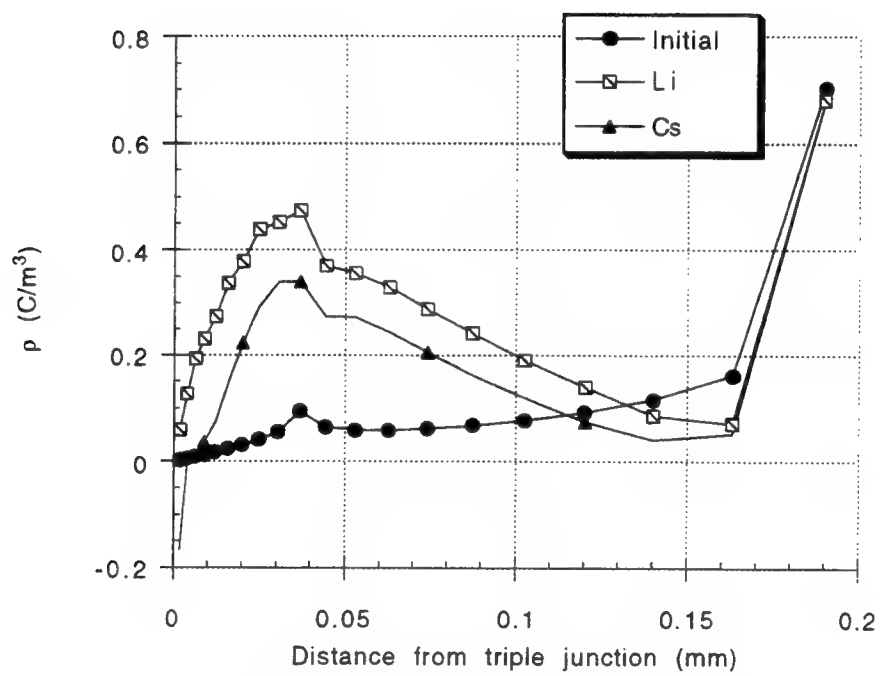


Figure 28: Surface charge density as a function of distance from the triple junction for different secondary electron yields, γ_{ee}

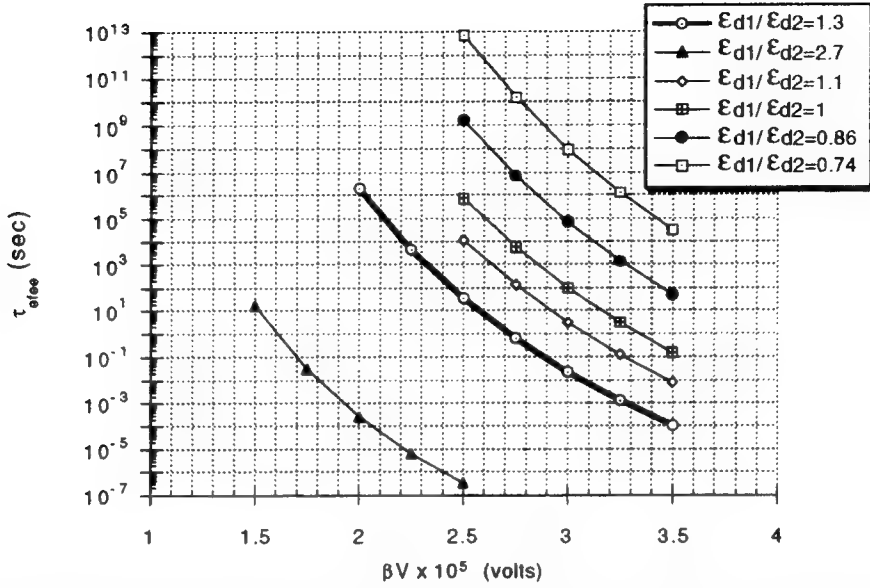


Figure 29: Enhanced field electron emission charging time, τ_{efee} , versus βV for different dielectric constant ratios

constants only directly affect ξ and ξ_0 . The ratio $\epsilon_{d_1}/\epsilon_{d_2}$ in Eq. (10) determines whether ξ_0 is less than, equal to, or greater than 1. Although this does not significantly affect the exponential factor of τ_{efee} , it does affect γ_{ee} through E_i as shown in Eq. (34).

The dielectric constants, however, significantly affect the surface charge density and consequently the secondary electron yield. Since $\epsilon_{d_1}E_1 = \epsilon_{d_2}E_2$, the ratio of dielectric constants, $\epsilon_{d_1}/\epsilon_{d_2}$, must equal the ratio of electric fields, E_2/E_1 . Therefore, if $\epsilon_{d_1}/\epsilon_{d_2}$ is greater than one, the electric field on the lower side surface will be higher. This higher electric field results in a higher surface charge density causing more electrons to be attracted and many more secondary electrons to be emitted. The electric field at the triple junction should then build up quite rapidly causing τ_{efee} to be relatively short. If $\epsilon_{d_1}/\epsilon_{d_2}$ is less than one, the electric field on the lower surface will be lower than the electric field on the upper surface, causing it to be very difficult for the electric field to build up at the triple junction. The EFEE charging time should then be very long.

The effect of the surface charge density is not accounted for, however, as the analytic expressions do not predict the large variation of τ_{efee} calculated by the numerical simulations. The results are shown in Figure 29. By increasing the ratio $\epsilon_{d_1}/\epsilon_{d_2}$ from the control case of 1.3 to 2.7, τ_{efee} decreases by about 7 orders of magnitude. By decreasing the ratio from 1.3 to 0.74, τ_{efee} increases by about 12 orders of magnitude. As expected, these results can be

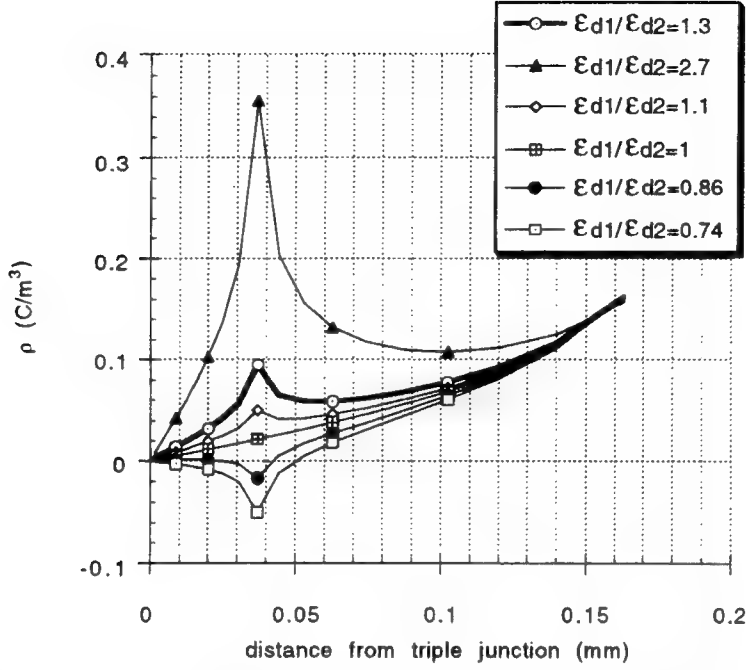


Figure 30: Dielectric side surface charge density before EFEE charging for different dielectric constants

explained by the surface charge density. The numerical results of the surface charge density calculations are shown in Figure 30. For higher values of $\epsilon_{d_1}/\epsilon_{d_2}$, the surface charge density is correspondingly high over the lower dielectric side surface. This attracts electrons, as shown in Figure 31, causing the electric field to run away in a short time. For the control case, the surface charge density does not build up as high before EFEE charging so $\tau_{e\text{f}ee}$ is longer. Correspondingly, the electron trajectories are not as concentrated near the triple junction, as shown in Figure 32. For cases with $\epsilon_{d_1}/\epsilon_{d_2} < 1$, the surface charge density over the lower dielectric side surface is negative before beginning EFEE charging so that electrons are repelled from the adhesive, as shown in Figure 33, causing secondary electron emission to be substantially reduced. For these latter cases the useful secondary electron yield is near or below 1, so that the electric field assumes a steady state which does not run away in any reasonable time.

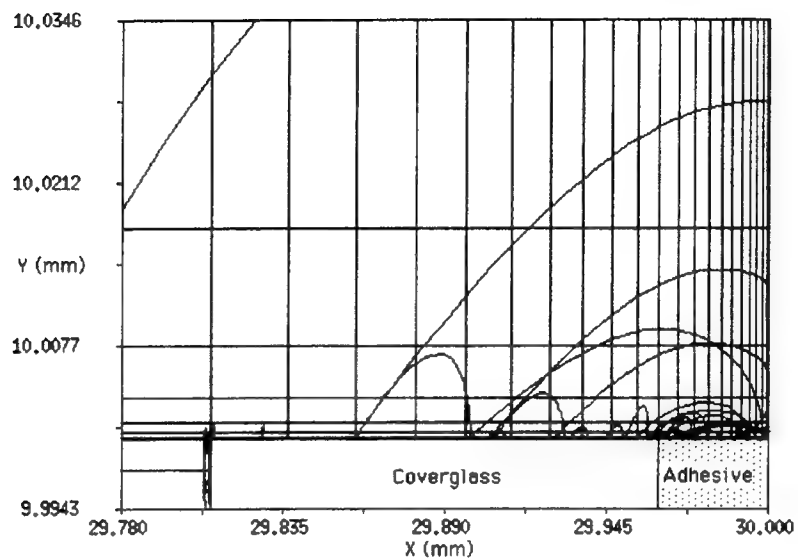


Figure 31: Electron trajectories for $\epsilon_{d_1}/\epsilon_{d_2} = 2.7$

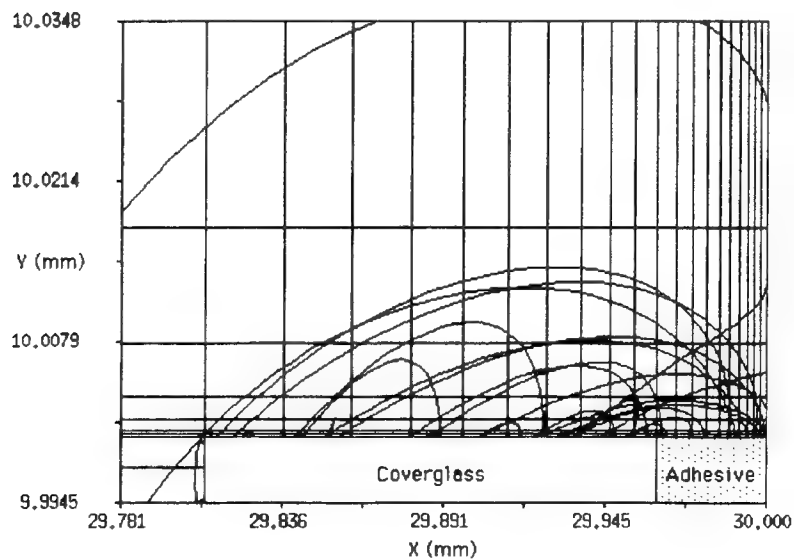


Figure 32: Electron trajectories for the control case of $\epsilon_{d_1}/\epsilon_{d_2} = 1.3$

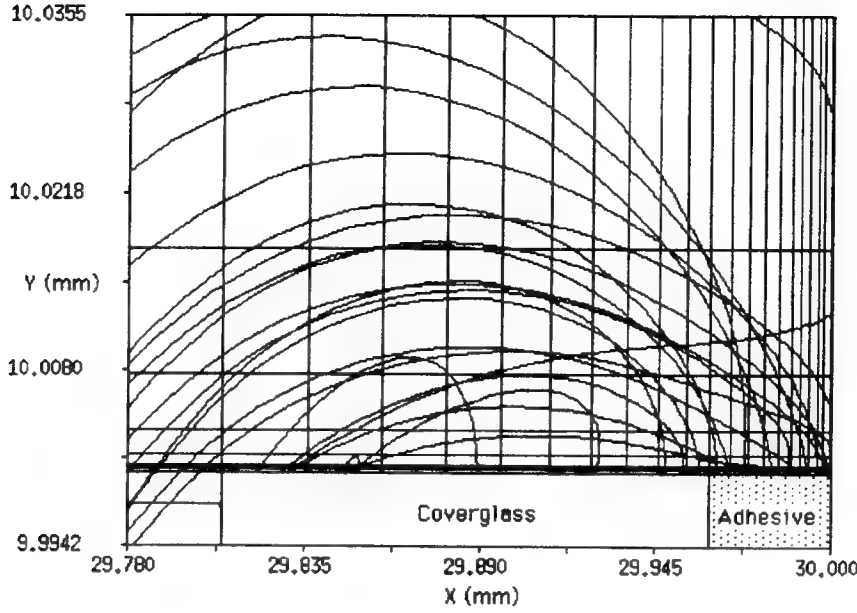


Figure 33: Electron trajectories for $\epsilon_{d_1}/\epsilon_{d_2} = 0.74$

The effects on the secondary electron yield as calculated by the numerical simulations can be seen in Figure 34. As expected from the surface charge density results, γ_{ee} for cases with $\epsilon_{d_1}/\epsilon_{d_2} < 1$ is significantly lower than for the other cases.

3.6 Overhanging the Coverglass

The final mitigation strategy studied involves lengthening the coverglass into an overhang over the interconnector to create a back surface, as shown in Figure 35, on which charge can accumulate. This method was expected to increase τ_{efee} since the overhang creates an additional surface over which the charge must build up for the electric field to run away.

3.6.1 Numerical Results

As shown in Figure 36, the results confirm this expectation. As the overhang is increased in length up to $30\mu\text{m}$, τ_{efee} is increased uniformly. In the βV range studied, this pattern changes for overhangs longer than $30\mu\text{m}$, indicating a different physical effect of the overhang on the EFEE charging time.

The difference between these two classes is clearly shown in Figure 37. The electric field at the triple junction E_{TJ} increases with time for the the first class, indicating a build up of charge due to EFEE and secondary electron emission. However, it decreases initially

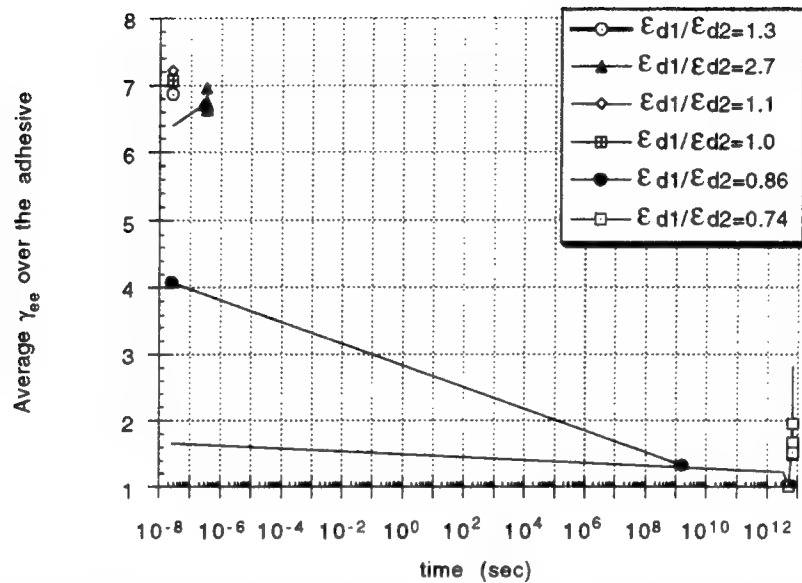


Figure 34: Average secondary electron yield over the adhesive versus time for different dielectric constants

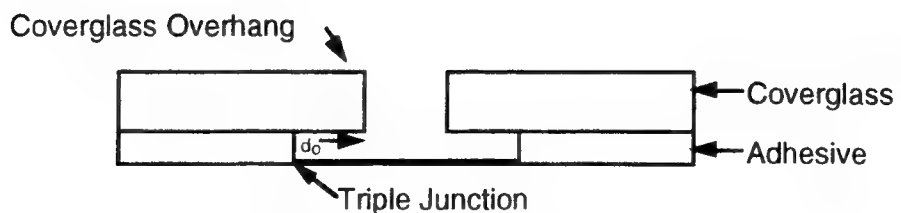


Figure 35: Model of coverglass overhang

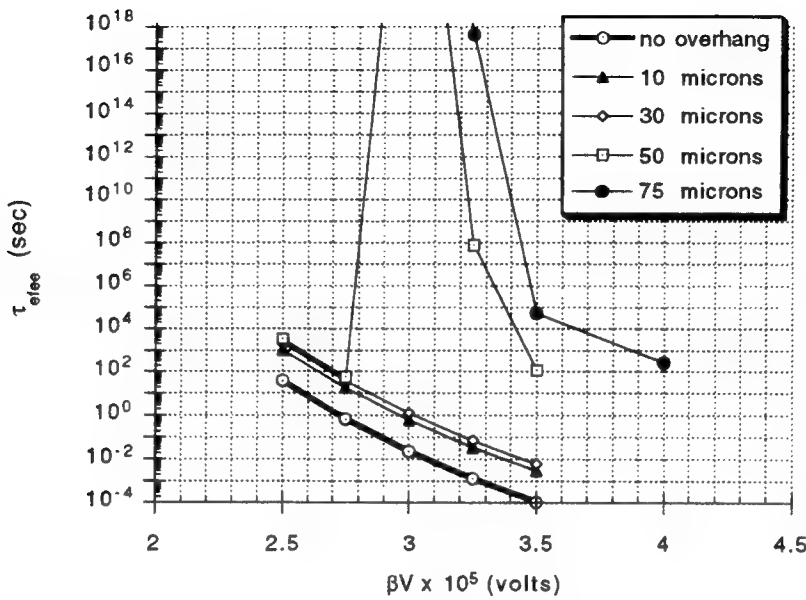


Figure 36: Enhanced field electron emission charging time, τ_{efee} , versus βV for different overhang lengths

before increasing, often drastically, for the second class, indicating an initial build up of negative charge from electron accumulation before electron emission from the side surface becomes high enough to create the positive charge build up necessary for runaway.

The corresponding effects of these differing electric fields on the electron trajectories can be seen in Figures 38 and 39. The first shows that the electrons in the first class of simulations are merely diverted by the overhang. The second shows that the electrons in the second class are mainly confined to the back surface with few arriving at the side surface of the coverglass. This shows that the first class of overhangs are acting as additional surface area while the second class are obstructing the electron trajectories to the side surface.

The potential along the surface reflects these electron trajectories. Figure 40 shows that for the first class the potential along the back surface increases with time, which causes the electric field at the triple junction to increase with time as well. For the second class, shown in Figure 41, the back surface potential initially decreases with time until it eventually increases at very large times. This initial potential decrease corresponds to the initial electric field decrease, indicating that the surface is charging negatively due to electron build-up rather than positively due to high secondary electron emission. This is clearly the case as shown in Figure 39, in which almost all of the electrons strike the back surface while very few reach the side surface. Hence, the large negative charge on and near the back surface

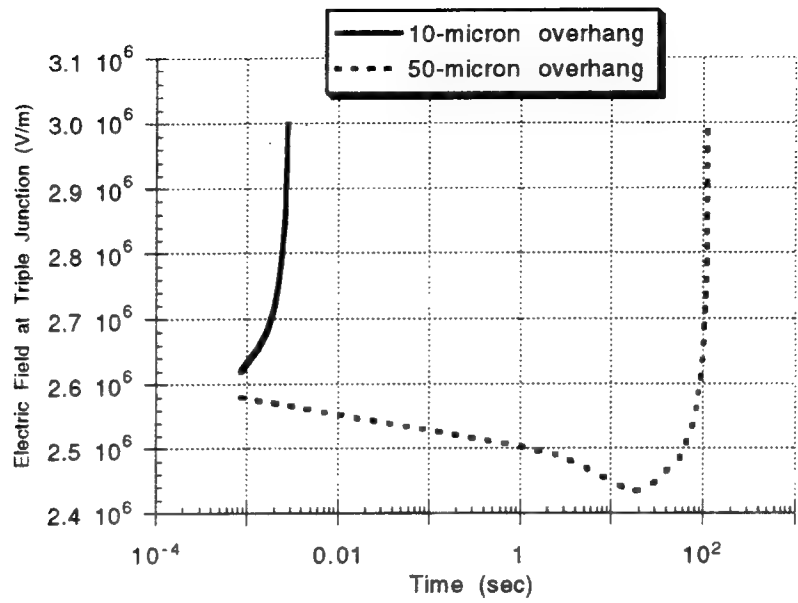


Figure 37: Class comparison of τ_{efee} versus E_{TJ} for $\beta V = 3.5 \times 10^5 \text{ V}$

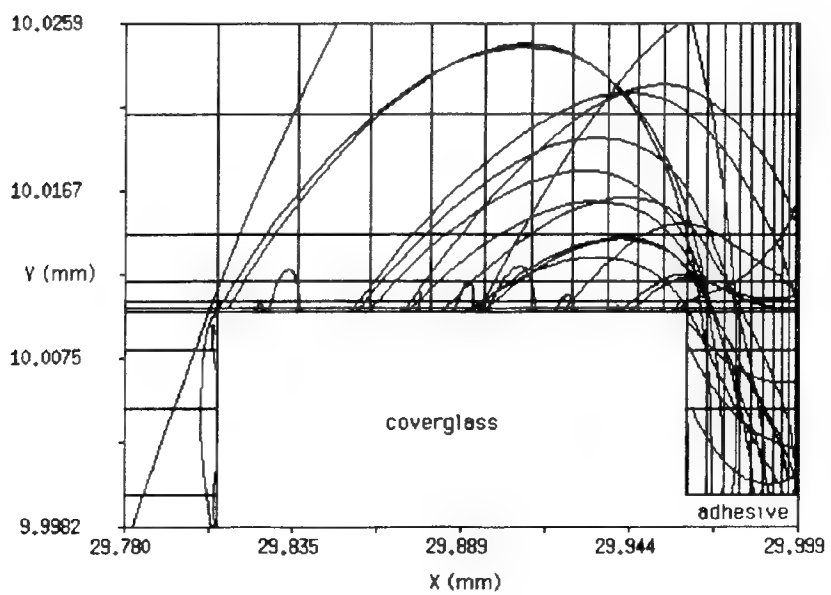


Figure 38: Electron trajectories for $10\mu\text{m}$ overhang; $\beta V = 3 \times 10^5 \text{ V}$

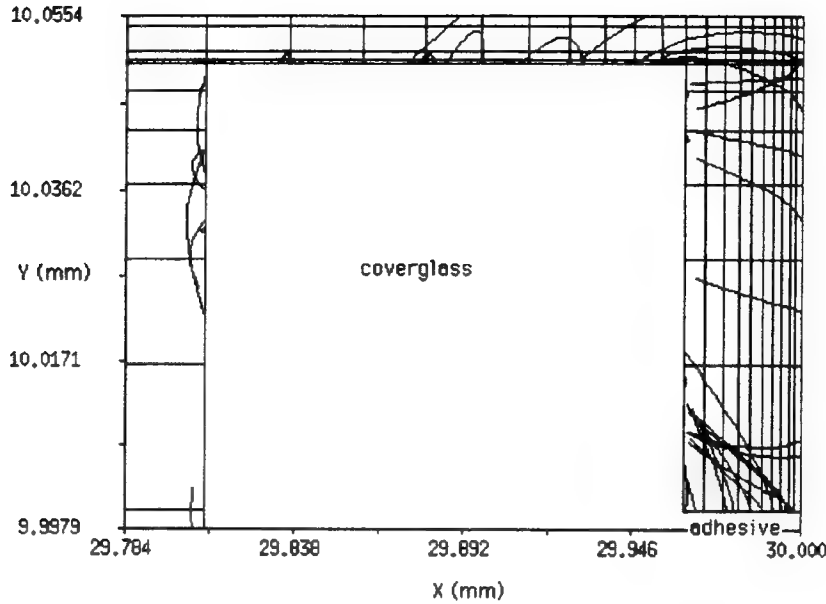


Figure 39: Electron trajectories for $50\mu\text{m}$ overhang; $\beta V = 3 \times 10^5 \text{ V}$

suppresses the electric field, causing it to decrease rather than increase.

3.6.2 Analysis

The results above suggest that there is a critical overhang which determines the behavior of the solution. Below this critical overhang, the electric field runaway is similar to the case of no overhang but at a lengthened time. Above it, the field initially decreases for a long time before building up to the runaway. Hence, coverglasses made longer than this critical overhang will have substantially reduced arcing.

Using the geometry shown in Figure 2, a simple calculation can determine the approximate critical overhang. Since the electric field is only orthogonal to the conductor and approximately orthogonal to the back surface, the free electron force balance is

$$m_e \frac{dv_x}{dt} = e E_x \quad (44)$$

and

$$m_e \frac{dv_y}{dt} \simeq 0, \quad (45)$$

where m_e is the electron mass, v_x and v_y are the electron velocities in the x and y directions respectively, and E_x is the electric field in the x direction.

Electrons emitted from the back surface follow ballistic trajectories according to this electric field. The time to the peak of each ballistic trajectory is

$$t = \frac{v_{x_0}}{e E_x / m_e}, \quad (46)$$

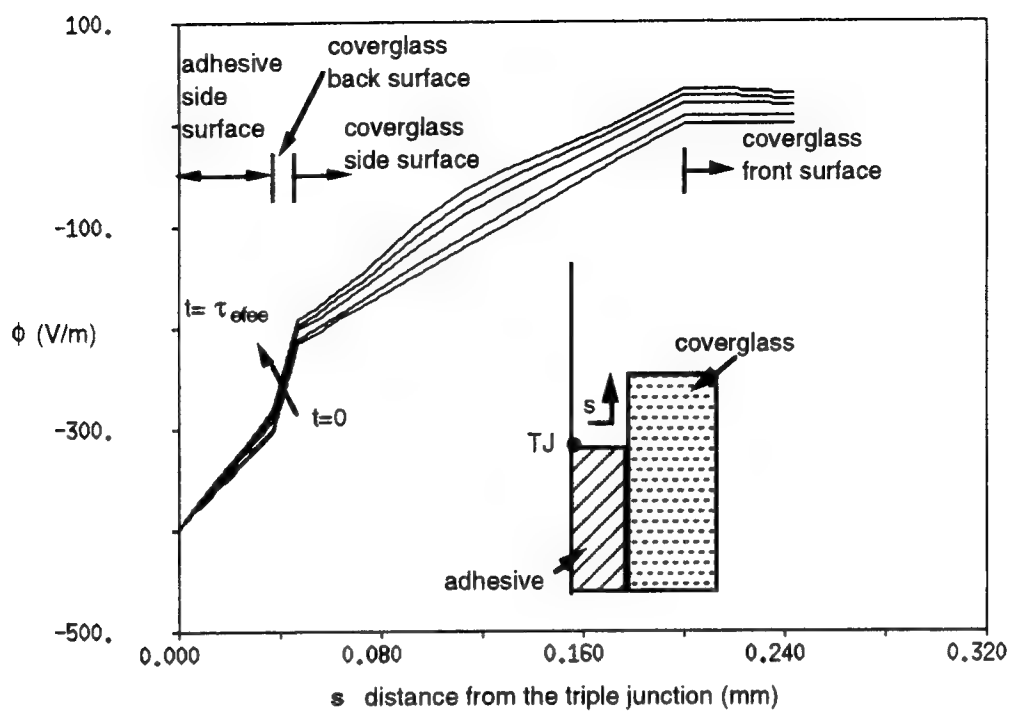


Figure 40: Class 1 dielectric surface potential; $\beta V = 3 \times 10^5 \text{ V}$, $d_o = 10 \mu\text{m}$

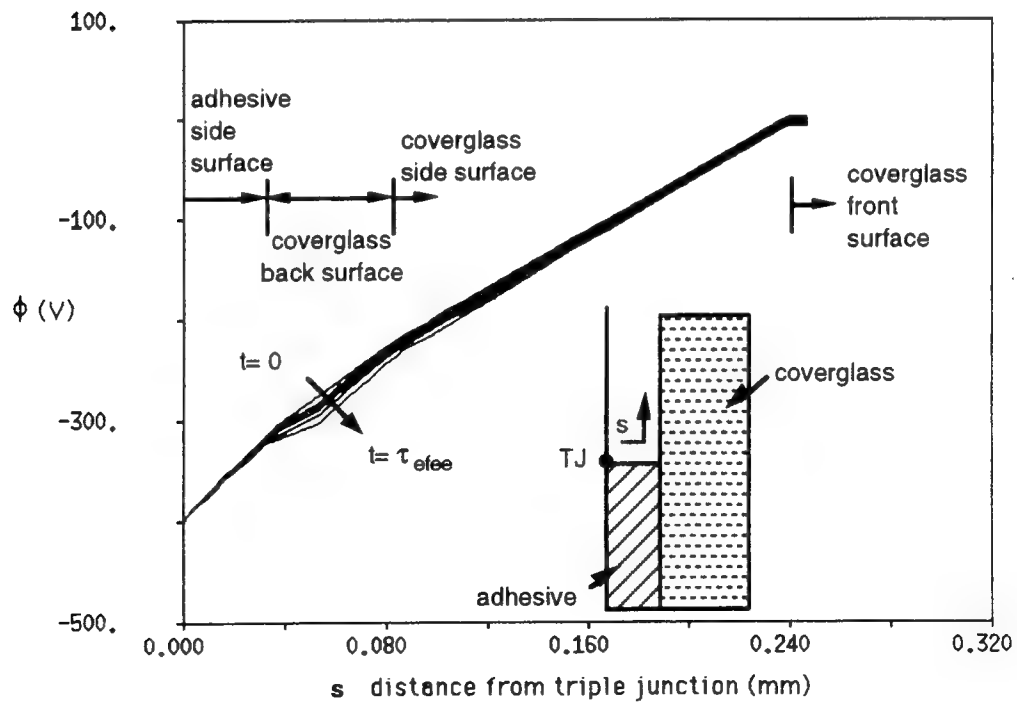


Figure 41: Class 2 dielectric surface potential; $\beta V = 3.25 \times 10^5 \text{ V}$, $d_o = 50 \mu\text{m}$

where v_{x_0} is the initial electron velocity in the x direction. The distance the electron travels along the back face before re-impacting the surface is

$$y_t = \frac{2v_{y_0}v_{x_0}}{eE_x/m_e}, \quad (47)$$

where v_{y_0} is the initial electron velocity in the y direction.

The electric field E_x can be found from the potential difference between the conductor and the back surface. Assuming the potential of the front surface is zero, the electric fields of the coverglass and adhesive can be expressed as

$$E_1 = \frac{\phi_i}{d_1} \quad (48)$$

and

$$E_2 = \frac{\phi_c - \phi_i}{d_2}, \quad (49)$$

where ϕ_i is the potential along the interface of the coverglass and adhesive and ϕ_c is the potential of the conductor, or interconnector. At the interface, $\epsilon_{d_1}E_1 = \epsilon_{d_2}E_2$. By substitution to eliminate ϕ_i and E_1 , both of which are unknown, the following expression is derived for E_2 , or E_x :

$$E_x = \frac{\phi_c}{d_2} \left(\frac{\epsilon_{d_1}d_2/\epsilon_{d_2}d_1}{1 + \epsilon_{d_1}d_2/\epsilon_{d_2}d_1} \right). \quad (50)$$

Since the critical overhang determines the behavior of the system, the differences between the two classes should be reviewed. For the first class, the electric field at the triple junction increases with time. This means that positive charge is accumulating on the back surface of the coverglass, as shown in Figure 40. Therefore the secondary electrons are escaping from the back surface, as shown in Figure 38. In contrast, in the second class of solutions the electric field is initially decreasing with time; therefore, negative charge is accumulating on the back surface of the coverglass, as shown in Figure 41, so secondary electrons cannot immediately escape the back surface, as shown in Figure 39.

Hence, the critical overhang that separates the two solutions can be bounded by requiring that the distance $y_t < d_o$ so that electrons cannot immediately escape and by requiring that the energy $m_e/2v_{y_0}v_{x_0}$ be bounded by the secondary electron emission energy for unity yield, \mathcal{E}_1 . This latter requirement means that an electron striking the back surface never has enough energy to release more than one electron. Therefore, the back surface must charge negatively. These two bounds give

$$\frac{d_o^c}{d_2} \leq \frac{4\mathcal{E}_1}{e\phi_c} \frac{1 + \epsilon_{d_1}d_2/\epsilon_{d_2}d_1}{\epsilon_{d_1}d_2/\epsilon_{d_2}d_1}. \quad (51)$$

For the conditions in Table 1, $\mathcal{E}_1 \approx 40\text{eV}$ and with $\phi_c = 400\text{V}$, Eq. (51) gives $d_o^c \leq 67\mu\text{m}$. This corresponds well with what is observed in Figure 36 where the $50\mu\text{m}$ overhang shows

the characteristics of both classes while the $75\mu\text{m}$ overhang shows only the characteristic of the second class.

This approximate expression can be further simplified in the limit $d_2 \ll d_1$ (which is usually the case). Eq. (51) then simplifies to

$$d_o^c \leq \frac{4\mathcal{E}_1 \epsilon_{d_2}}{e\phi_c \epsilon_{d_1}} d_1. \quad (52)$$

This shows that one can obtain the smallest critical overhang by reducing d_1 as much as possible, consistent of course with the need to maintain radiation protection, and by modifying the secondary electron emission properties of the coverglass so as to reduce the energy at which the yield is unity.

3.7 Arc Rate Results

The arc rates are determined by using the analytical model discussed in Section 2.1.2, as explained for the control case. This model is limited by the analytic expressions, which are only approximations of real processes and effects. For the results in the previous section which are consistent with the analytic predictions, the model is used with the varying parameters. For the secondary electron yield, dielectric constant, and overhang effects on $\tau_{e\text{fee}}$, which are not fully accounted for in the analytic expression, the model is used with $\tau_{e\text{fee}}$ modified according to the results from the numerical simulations.

The results are shown in Figures 42-46. In all cases the curves saturate around 350sec^{-1} , where the arc rate is limited by τ_{ion} which is not as dependent on voltage as is $\tau_{e\text{fee}}$. The goal of the mitigation strategies can clearly be seen, then, as increasing the voltage range of $\tau_{e\text{fee}}$ dominance.

The effect of different work functions on the arc rate is shown in Figure 42. None of the work functions significantly affect the arc rate, although the higher work functions do not arc at -200V. Also, little difference is seen between the arc rates of commonly used Kovar and silver interconnectors.

The thickness variations show a greater effect on the arc rate, especially for the smaller thicknesses between -200V to -400V. For a $118\mu\text{m}$ thickness of the coverglass and adhesive dielectrics, the arc rate is almost saturated at -300V, while the control case thickness of $190\mu\text{m}$ does not saturate until -600V. Increasing the thickness to $200\mu\text{m}$ or even $226\mu\text{m}$ eliminates arcing at -200V but does not reduce arcing significantly at higher voltages.

The effect of the secondary electron yield on the arc rate is shown to be significant only when the electric field does not run away, as in the $\gamma_{ee} = 0.7\text{-}1.2$ case. Even for the two cases (BeO and Li) which have secondary electron yields near and below unity, the arc rate

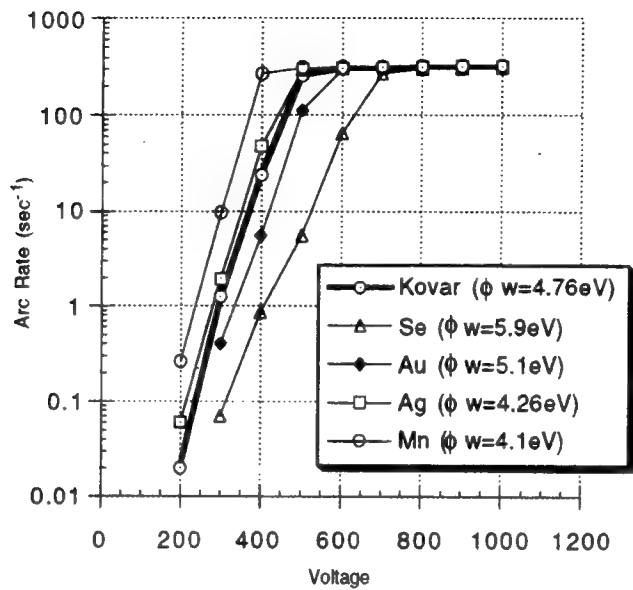


Figure 42: Analytic arc rates for varying interconnector work functions, ϕ_w

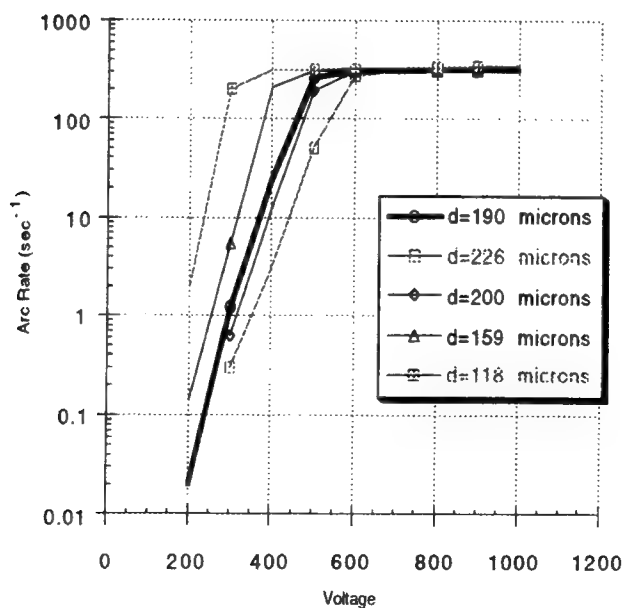


Figure 43: Analytic arc rates for varying dielectric thicknesses, d

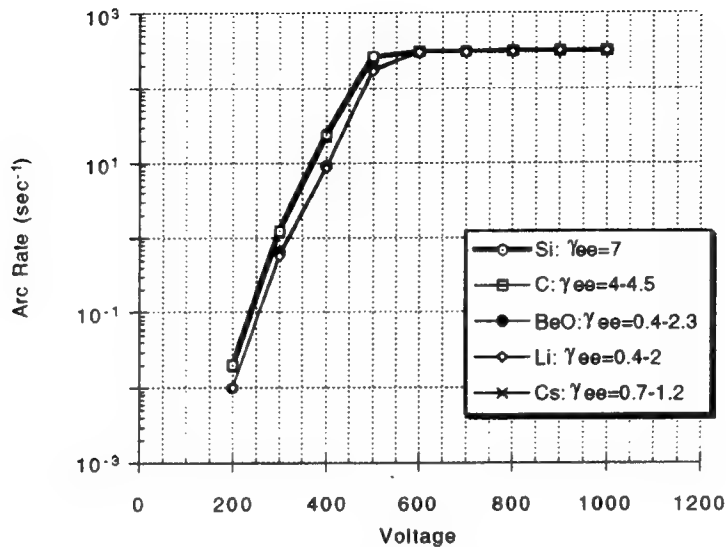


Figure 44: Predicted arc rates for varying secondary electron yields, γ_{ee}

is just barely reduced from the control case. Any secondary electron yield not near unity, such as that of carbon ($\gamma_{ee} = 4-4.5$), did not change the arcing rates at all from the control case of $\gamma_{ee} = 7$.

The dielectric constant variations and coverglass overhang cases show the largest effect on the arc rate. For the $\epsilon_{d_1}/\epsilon_{d_2} = 2.7$ case, the arc rate is almost saturated at -300V. For the case of equal dielectric constants, however, the arc rate does not saturate until -900V. For variations of $\epsilon_{d_1}/\epsilon_{d_2} < 1$ the arc rate is reduced significantly. No arcing is predicted until -600V for the $\epsilon_{d_1}/\epsilon_{d_2} = 0.74$ case.

For the coverglass overhang arc rates, the two different classes can be seen clearly in Figure 46. The arc rates of the first class do not decrease much even with an overhang of $30\mu\text{m}$, but the arc rates of the second class are significantly reduced. The $75\mu\text{m}$ case, which is beyond the critical overhang for the cell studied, shows no arcing until -600V and does not reach the saturation level in the range of voltages examined.

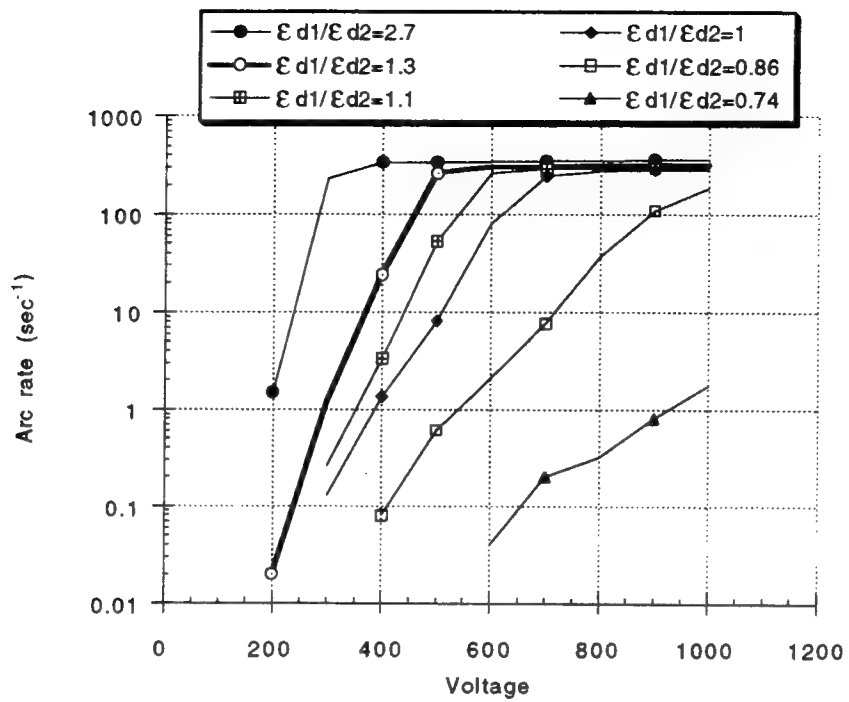


Figure 45: Predicted arc rates for varying dielectric constant ratios, $\epsilon_{d_1}/\epsilon_{d_2}$

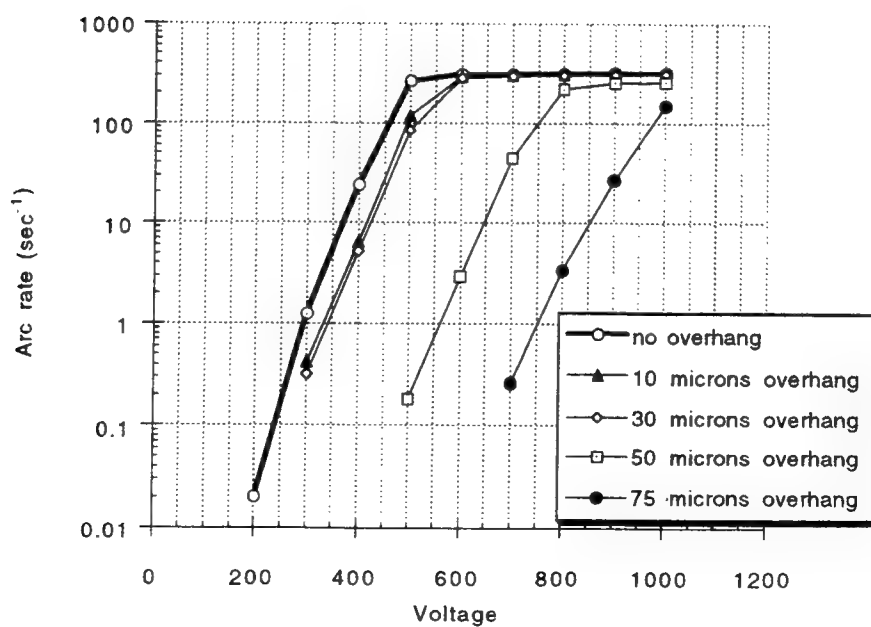


Figure 46: Predicted arc rates for varying coverglass overhang lengths, d_o (μm)

Chapter 4

PASP Plus Predictions

In March, 1994, the Solar Array Module Plasma Interactions Experiment (SAMPIE) was flown aboard the Space Shuttle. In the next few years, three more space missions are planned to study high voltage solar arrays, including the Photovoltaic Array Space Power Plus Diagnostics (PASP Plus) experiment. By using the numerical and analytical models for the conventional and wrap-through-contact cells, arcing predictions were made for the PASP Plus mission to aid in its preparation and to further check the validity of these models.

4.1 PASP Plus

PASP Plus is designed to provide the Air Force with important information regarding higher power space systems. Since greater spacecraft power will be required, the Air Force anticipates using advanced high voltage solar arrays and power distribution systems. The environmental interaction hazards of these systems therefore need to be determined to improve the reliability of future missions. To accomplish its task, the PASP Plus experiment includes both advanced solar arrays and a number of diagnostic instruments. PASP Plus has four main objectives²⁰:

- (1) characterize the electrical performance and the environmental interaction of advanced solar array designs operating at high voltages in the ionosphere and magnetosphere;
- (2) determine the long-term radiation degradation effects of several advanced solar arrays;
- (3) determine the impact of the space environment on solar array operation for various solar cell technologies; and
- (4) obtain flight performance data for advanced array designs never before flown.

4.2 Experiment Description

The PASP Plus experiment will be flown on the Advanced Photovoltaic and Electronics Experiments (APEX) satellite, scheduled to be launched in the summer of 1994 aboard the Pegasus launch vehicle. The satellite should reach an orbit of 1950km apogee, 360km perigee, and 70° inclination. Throughout the orbit, the spacecraft will be continuously sun pointing. The experiment is expected to last one year minimum and three years nominal.

The APEX spacecraft in its deployed configuration is shown in Figure 47. The arrays are located on the top shelf and on one of the deployed panels. The other three panels are the solar arrays needed for the spacecraft power system. Beneath the payload shelf is the avionics shelf, where most of the diagnostic instruments are located. There are three types of sensors to obtain array performance data and five types of sensors to characterize the space environment around the spacecraft. To calibrate the performance of the solar arrays, the following instruments will be used: a sun sensor to measure the incidence angle, meters to measure the current and voltage, and sensors near each array to measure the temperature. Instruments which characterize the space environment include a transient pulse monitor for measuring electromagnetic interference, a langmuir probe with sense potential capability for measuring the thermal plasma temperature and density, a dosimeter for measuring ion and electron radiation, an electrostatic analyzer to determine electron and ion spectra of moderate energy (10eV - 30keV), and five monitors for determining the amount of degradation due to radiation and the amount due to contamination. The spacecraft also contains a voltage generator capable of biasing the arrays at multiple high voltage levels, an electron emitter which will enable the satellite's potential to be altered, and an electronics controller for satellite operation.

Seventeen arrays of twelve different types will be mounted on the payload shelf and the deployed panel. Since there are only 16 electrical channels, one of the arrays will not be used. Ten of these arrays will be subject to multiple voltage biasing. The arrays, as well as the instruments described above, are all numbered for identification. They will be therefore introduced in order of their instrument numbers, and the biased arrays will then be described in further detail, with the exception of the concentrator arrays which are not included in this research. Arrays #0, #1, and #2 contain silicon conventional cells. The silicon WTC cells designed for Space Station Freedom make up array #3. Arrays #4 - #6 are Applied Solar Energy Corporation's (ASEC) gallium arsenide/germanium (GaAs/Ge) conventional cells, but array #5 will not be used so that its channel can be used by the APSA cell array. The advanced solar cells of AlGaAs/GaAs Monolithic MBG are on array #7. Spectrolab's

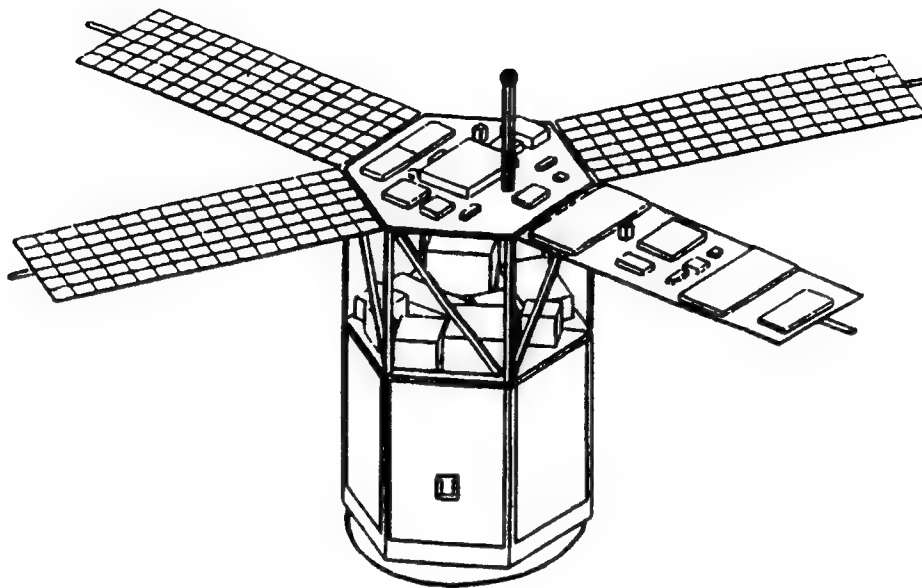


Figure 47: Deployed APEX spacecraft with PASP Plus experiment payload

WTC GaAs/Ge cells are located on array #8. Array #9 contains the amorphous silicon cells developed by TRW and Solarex. Another advanced solar cell, indium phosphate (InP), is on array #10. The conventional GaAs/Ge cells made by Spectrolab are on array #11. Another MBG cell, Boeing's GaAs/CuInSe solar cell, make up arrays #12 and #13. The Mini-Cassegrainian GaAs cell created at TRW will be on array #14 to accompany the newer Mini-Dome Fresnel Concentrator created at Boeing which is on array #15. Finally, the APSA cell was added late to the list so its array is #36.

The silicon conventional arrays #1 and #2 are the first biased arrays, containing 20 and 60 cells respectively. Originally built by RCA in 1984, these cells are included to be representative of present operational space flight solar cells. Also, they were not designed to withstand high voltage operation. The cells are $2\text{cm} \times 4\text{cm}$ and $203\mu\text{m}$ (8mil) thick. The coverglass is fused silica and the cover adhesive is DC 93500, of estimated thickness $153\mu\text{m}$ (3mil) and $37\mu\text{m}$ (1.5mil) respectively. The interconnector is assumed to be Kovar, which has an estimated work function 4.76eV.

The Space Station Freedom array of 4 cells (#3) will also be biased. These WTC cells were designed to operate in low earth orbit at a 160V nominal operating voltage. The $8\text{cm} \times 8\text{cm}$ cells are $203\mu\text{m}$ (8mil) thick. As discussed in Section 2.2, the cells are covered

with a ceria-doped borosilicate coverglass and a Kapton substrate.

Arrays #4 and #6 of ASEC's GaAs/Ge conventional cell design are comprised of 20 and 12 cells respectively, and both will be biased. These cells were designed to have high radiation resistance and high cell efficiency, making them representative of the standard for the next generation of satellite photovoltaic power. The $4\text{cm} \times 4\text{cm}$ cells have a thickness of $76\mu\text{m}$ (3.5mil) and CMX coverglasses of $102\mu\text{m}$ (4mil). The interconnector is silver-plated invar so the relevant work function is that of silver, which is 4.26eV.

Both of Spectrolab's arrays, #8 and #11, will be biased. The first array is their WTC design, which is expected to operate better than conventional cell designs at high voltages. The $4\text{cm} \times 4\text{cm}$ cells, which are $177\mu\text{m}$ (7mil) thick, are covered by a $152\mu\text{m}$ (6mil) thick coverglass and mounted on a Ge substrate. The second array contains a similar cell of conventional design. The dimensions of both the cell and coverglass are the same, and the adhesive is estimated to be $76\mu\text{m}$ (3mil) thick. Like the ASEC GaAs/Ge cells, these cells also have a silver-plated invar interconnector.

The Advanced Photovoltaic Solar Array (APSA) is the final high voltage biased array studied. These thin-film silicon cells are expected to be the cells of the future, based on the mass cost savings they yield. Built by TRW, they are $2.6\text{cm} \times 5.1\text{cm}$ of only $56\mu\text{m}$ (2.2mil) thickness. More importantly for arcing considerations, the cell CMX coverglass thickness is merely $51\mu\text{m}$ (2mil) thick and the DC 93500 cover adhesive is estimated to be $76\mu\text{m}$ (3mil) thick. The interconnector is again silver-plated invar.

The voltage biasing will be performed in pre-set sequences from -500V to +500V, with each bias step held for 23 seconds. In this work, predictions were made at 25 volt increments with a twenty second experiment time.

4.3 Predictions

To predict the arcing rate of the biased arrays, the analytic arc rate method described in Section 2.1.2 is used. Table 2 shows the given and assumed cell properties necessary for the arc rate calculations. To determine C_{diele} and the offset of τ_{efee} due to the surface charge density (see Section 3.4), the numerical model must be run initially. Only the first scheme, the capacitance matrix method, is necessary to determine the polynomial fit for C_{diele} . Since the surface charge density is not incorporated into the analytic model, an offset of $\tau_{efee}(\text{numerical})$ versus $\tau_{efee}(\text{analytical})$ must be accounted for. The case chosen by Cho³ closely matches the numerical and analytical τ_{efee} values. Since τ_{efee} versus βV curves have the same shape, the best technique is to determine the offset of each curve

Table 2: PASP Plus data used for arc rate predictions

Instrument No.	1, 2	3	4, 6	8	11	36
Cell Type	Si	Si WTC	GaAs/Ge	GaAs/Ge WTC	GaAs/Ge	APSA
Manufacturer	RCA	NASA	ASEC	Spectrolab	Spectrolab	TRW
Cell Size (cm ²)	2x4	8x8	4x4	4x4	4x4	2.6x5.1
No. of Cells	20, 60	4	20, 12	4	8	12
Cell Gap (μm)	500	1000	500	1000	500	635
d_{cell} (μm)	203	203	89	178	178	56
d_1 (μm)	153	203	102	152	152	51
d_2 (μm)	37	N/A	51	N/A	76	76
ϵ_{d_1}	3.5	4	4	4	4	4
ϵ_{d_2}	2.7	3	2.7	3	2.7	2.7
γ_{max_1}	3.46	4	4	4	4	4
γ_{max_2}	3	2	3	2	3	3
E_{max_1} (eV)	330	400	400	400	400	400
E_{max_2} (eV)	300	200	300	200	300	300
ϕ_w (eV)	4.76	4.85	4.26	4.5	4.26	4.26

from the case that can be accurately predicted analytically. Therefore, the entire numerical model is used at a specified voltage with the orbit integration scheme run for several β values, typically five, to determine this offset.

The orbital data for the analytical model requires a different approach. Since the orbit is neither circular nor of constant altitude, the orbital parameters must be determined for each point along the orbit at which the arc rate is to be calculated. The International Reference Ionosphere (IRI) program, developed at Goddard Space Flight Center in June 1987, can calculate the ambient density n_e , the electron temperature T_e , and the ion mass m_i if given the altitude, month, hour, sunspot number, and the geodetic coordinates. Since the exact time of the biasing is unknown, the parameters are averaged over the entire year by hour and by month. The times that gave the lowest and highest ambient densities are also used to define the lowest and highest arcing rates which might be observed. The variation due to different sunspot numbers is within the variation due to ambient densities. To determine the coordinates, as well as the altitude and orbital velocity, a separate calculation is necessary. Orbital mechanics are used to find the state vector in inertial coordinates of a given altitude. These are then converted to the earth-fixed coordinates. By using the orbit inclination,

longitude of the ascending node and the orbital eccentricity, the equations of motion can be integrated using a fourth-order Runge-Kutta method to obtain other positions along the orbit.

At altitudes higher than 1000km, the IRI model is useless for obtaining particle densities. At these altitudes, however, the following formula developed by Al'Pert¹ has been shown to agree well with experimental measurements:

$$n_e(z) = n_{e_0} \frac{z_0}{z} \exp \left[\frac{g_0 M_o z_0}{2kT_{e_0}} \left[\frac{1}{1 + \frac{R_o}{z}} - \frac{1}{1 + \frac{R_o}{z_0}} + \ln \left(\frac{1 + \frac{R_o}{z}}{1 + \frac{R_o}{z_0}} \right) \right] \right]. \quad (53)$$

In this equation R_o is the Earth's mean radius, n_{e_0} is the electron density at 1000km, g_0 is the gravitational acceleration at 1000km, M_o is the mass of hydrogen at 1000km, T_{e_0} is the electron temperature at 1000km, and z_0 is the altitude of 1000km. Finally, the arc rate program requires the input of a range of electron densities. Since each voltage bias will be held for 23sec, the electron densities at either end of that range along the orbit are used to define the maximum and minimum densities expected.

For each array arc rates are predicted for voltages up to -500V in 25V increments at intervals of 600sec around the orbit. Near apogee, the spacecraft slows and the arcing rates have less variation due to the lower ambient densities so the intervals are increased to 1200sec.

The arc rate results for the conventional arrays are presented in Figures 48-59. For each array, the first figure shows representative arc rates around the spacecraft orbit for the entire voltage range. Standard deviation error bars included on these figures are based on typically 100 calculations for each voltage. The arc rates at lower voltage biases are identical since $\tau_{e\text{fee}}$ is dominant. The diverging curves at higher voltages indicate τ_{ion} is beginning to affect the arc rates. To distinguish the arc rates at these higher voltages, a second figure for each array shows all of the arc rate curves in the τ_{ion} range. As shown in Figure 48, the arc rates for the silicon conventional array with 20 cells range from an average of 0.004sec^{-1} at 200V to 211sec^{-1} at 500V. At 500V bias, the arcing rates are as low as 8.75sec^{-1} , which is calculated at apogee. The addition of 40 more solar cells to the array increases the number of emission sites where arcing can occur, thus decreasing the time between arcs. This is clearly seen in Figure 50, which shows that arcing begins at voltages as low as 175V for array #2. The highest arcing rate calculated is 366sec^{-1} at perigee for a voltage bias of 500V, while at apogee the arcing rate is 33sec^{-1} . For ASEC's GaAs/Ge array of 20 cells (#4), arcing is predicted at 125V, as shown in Figure 52. Accordingly, the arcing rates are much higher at 500V, with a maximum of 1382sec^{-1} and a minimum of 50sec^{-1} . The slightly smaller array of only 12 cells (#6) is also predicted to experience arcing at 125V.

but its arcing rates at 500V range from 918sec^{-1} to only 33sec^{-1} . The arc rate predictions, shown in Figure 56, for Spectrolab's GaAs/Ge array of 8 cells are significantly lower than predictions for ASEC's GaAs/Ge array. Arcing is not predicted until 175V, and arc rates at 500V are at most 69sec^{-1} (at perigee) and at least 15sec^{-1} (at apogee). The thin APSA is predicted to experience arcing at the low voltage of 100V in the lower altitudes. The high arcing rates, however, are not nearly as high as for arrays #4 and #6. The lower arc rates are much higher, indicating a higher $\tau_{e\text{fee}}$, but the arc rates saturate around 300V by τ_{ion} . Consequently at 500V, the highest arc rate is predicted to be only 413sec^{-1} and the lowest is predicted to be 15sec^{-1} .

To compare these results, Figure 60 shows the arc rate predictions for each conventional array at perigee. The GaAs/Ge arrays and APSA only differ in $\tau_{e\text{fee}}$ properties in dielectric thickness (See Table 2). As expected, the thin APSA has the highest arc rate predictions in the $\tau_{e\text{fee}}$ -dominated range, with only $127\mu\text{m}$ dielectric thickness. Spectrolab's GaAs/Ge cells with $228\mu\text{m}$ thick dielectrics have the lowest predicted arc rates, and ASEC's GaAs/Ge cells with $153\mu\text{m}$ thick dielectrics are predicted to experience arcing of intermediate intensity. All of these arrays have silver-plated interconnectors, in contrast with the Kovar interconnectors of the silicon cells. From the arc rate sensitivity study of different interconnector work functions in Chapter 3, however, the difference in arc rates between these two metals is negligible (see Figure 42). The silicon cells also have $190\mu\text{m}$ thick dielectrics, which is between the thicknesses of Spectrolab's GaAs/Ge cells and ASEC's GaAs/Ge cells. The predicted arc rates of the silicon arrays also fall between the arcing rates of those arrays, so the dielectric thicknesses must be the discriminating factor among all of the arrays for the range dominated by $\tau_{e\text{fee}}$. For the range dominated by τ_{ion} , the major difference between the arrays is the cell frontal area, A_{cell} . According to Eq. (6) the smaller APSA cells increase τ_{ion} , thus decreasing the arc rate saturation level from that of the larger cells.

To predict the arc rates of the WTC cell arrays, an analytical model similar to the one for the conventional cell arrays should be used. This model has not yet been determined so the arc rate predictions for this cell design are left for future work.

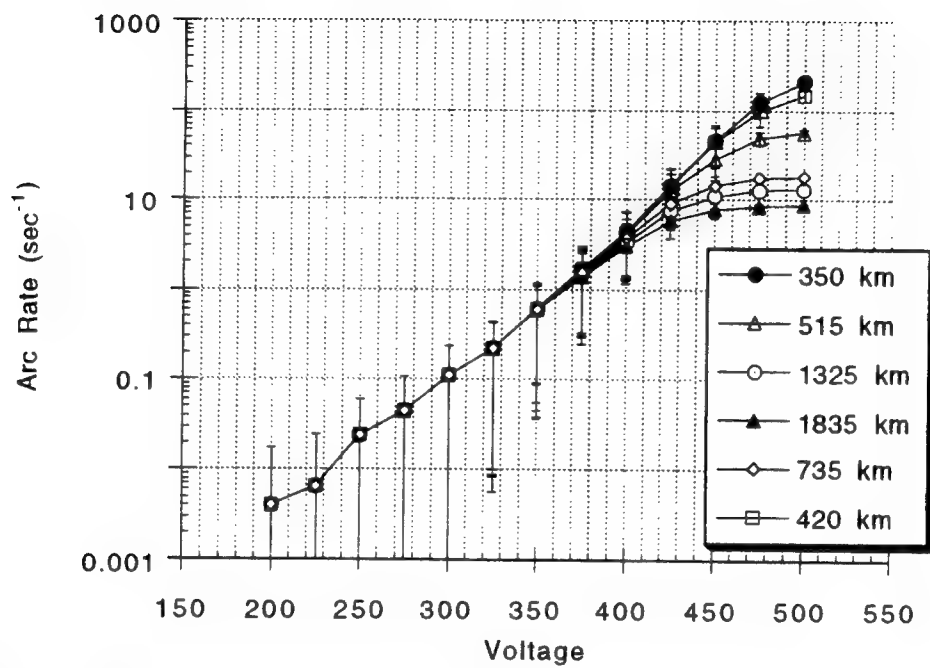


Figure 48: Selected arc rate predictions with standard deviation errors for Si conventional array #1

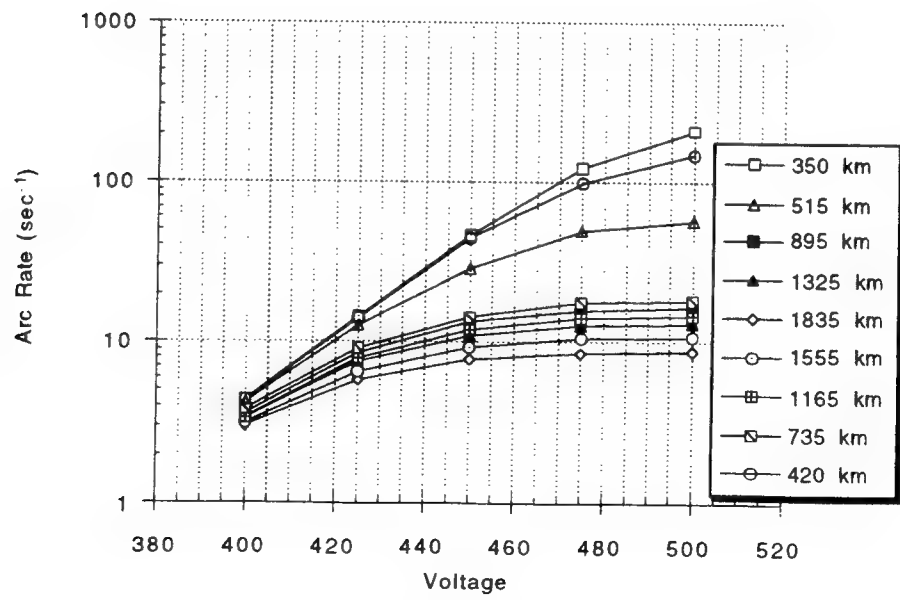


Figure 49: Complete arc rate predictions in the differentiating voltage range for Si array #1

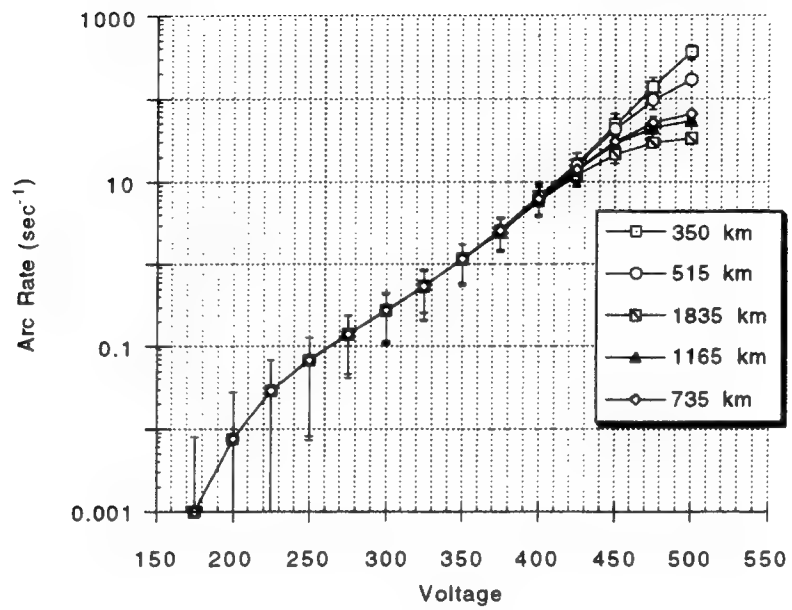


Figure 50: Selected arc rate predictions with standard deviation errors for Si conventional array #2

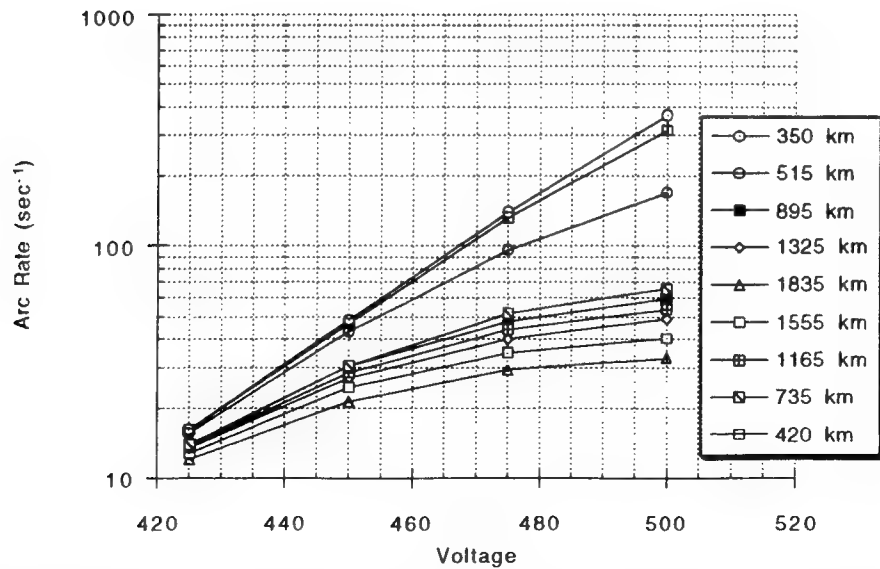


Figure 51: Complete arc rate predictions in the differentiating voltage range for Si array #2

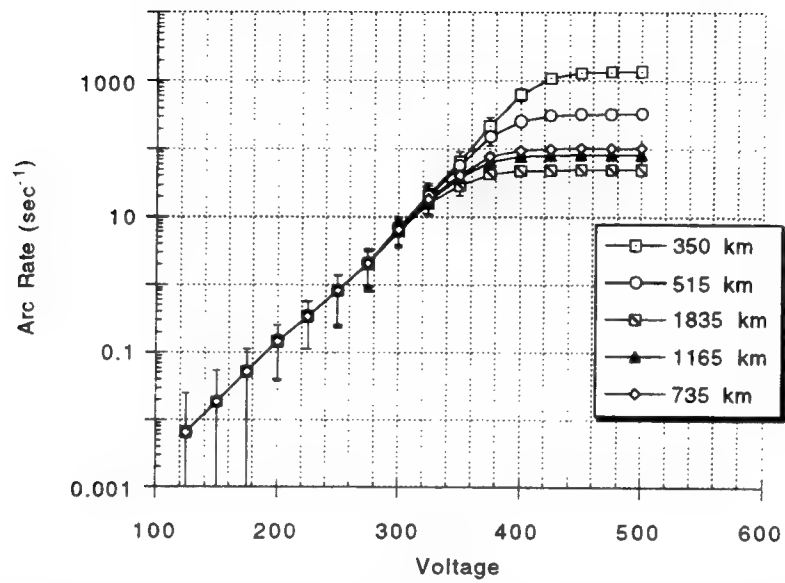


Figure 52: Selected arc rate predictions with standard deviation errors for GaAs/Ge conventional array #4

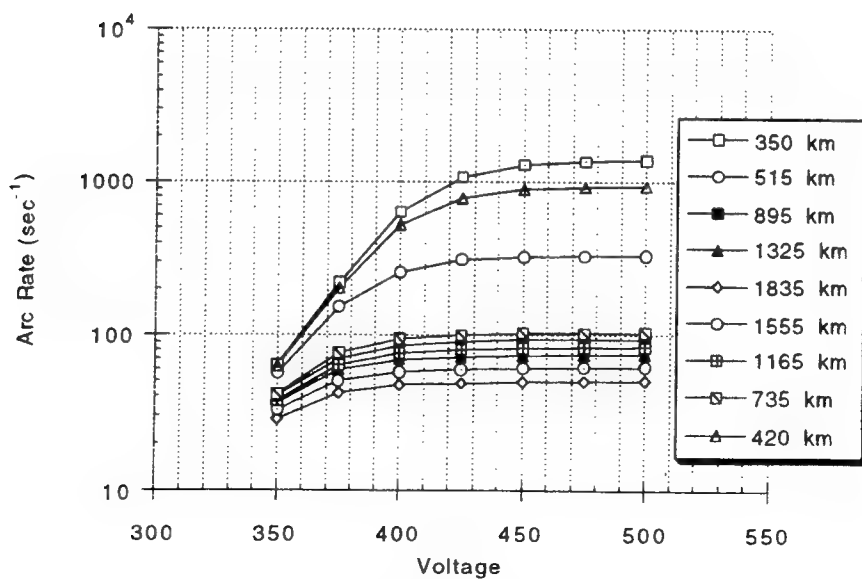


Figure 53: Complete arc rate predictions in the differentiating voltage range for GaAs/Ge array #4

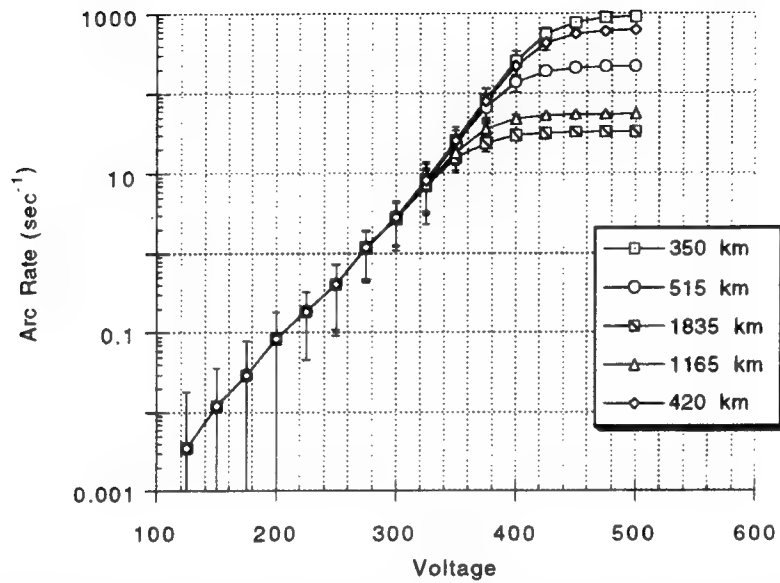


Figure 54: Selected arc rate predictions with standard deviation errors for GaAs/Ge conventional array #6

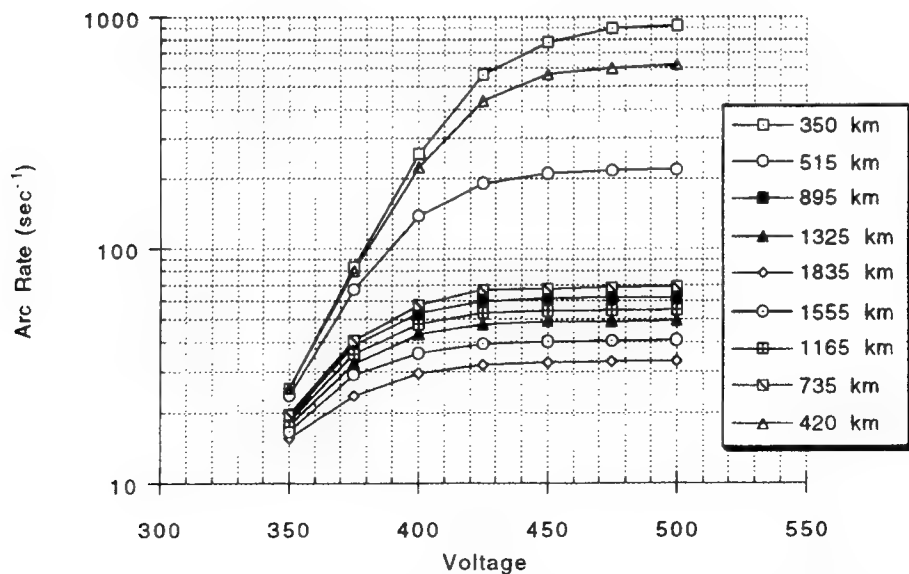


Figure 55: Complete arc rate predictions in the differentiating voltage range for GaAs/Ge array #6

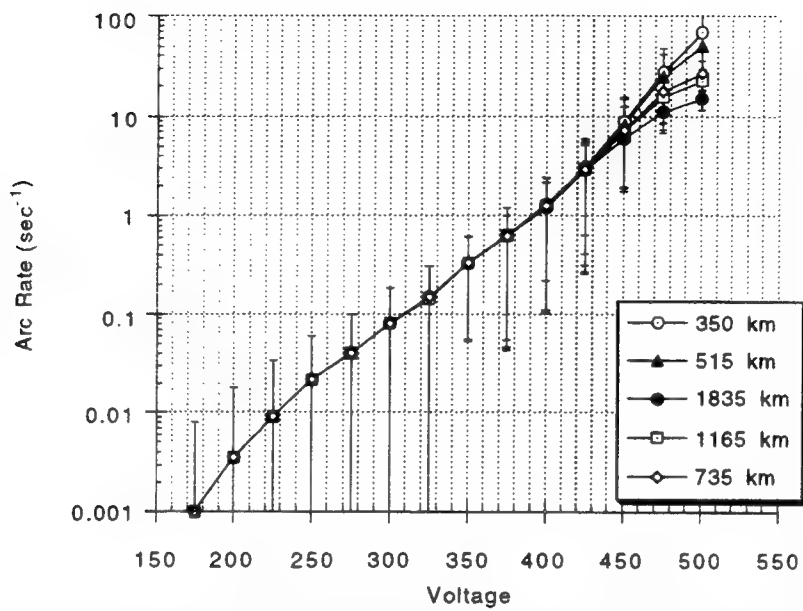


Figure 56: Selected arc rate predictions with standard deviation errors for GaAs/Ge conventional array #11

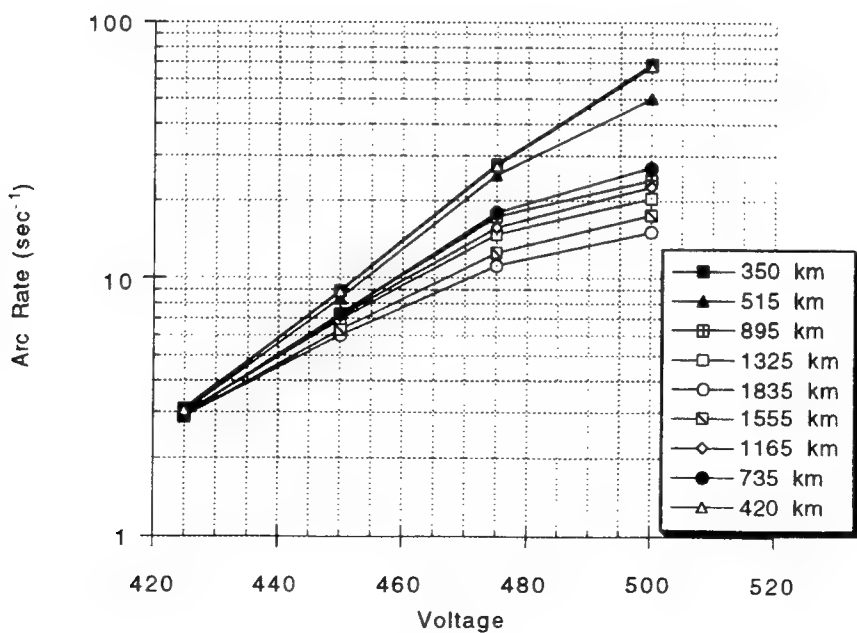


Figure 57: Complete arc rate predictions in the differentiating voltage range for GaAs/Ge array #11

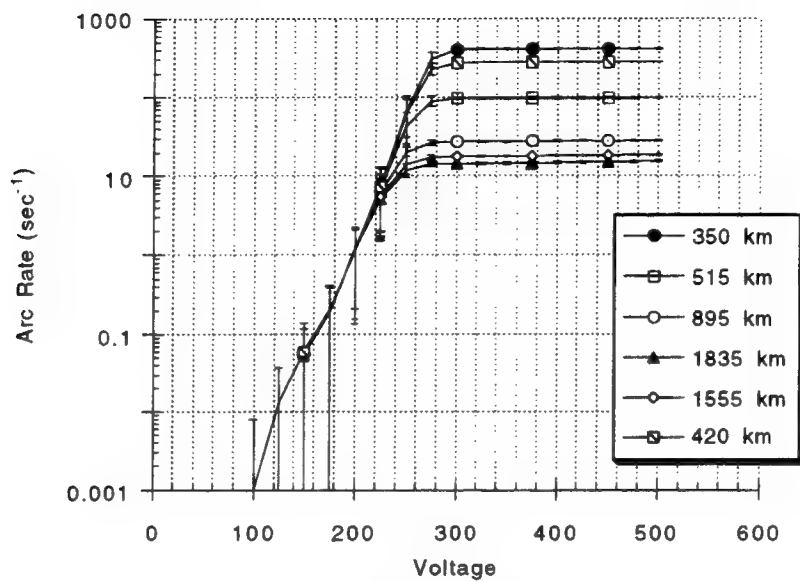


Figure 58: Selected arc rate predictions with standard deviation errors for APSA (#36)

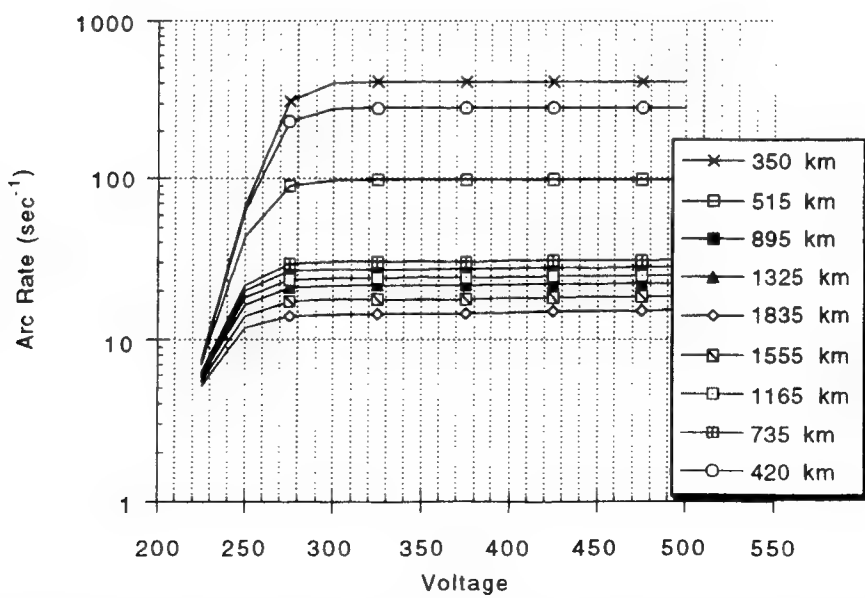


Figure 59: Complete arc rate predictions in the differentiating voltage range for APSA (#36)

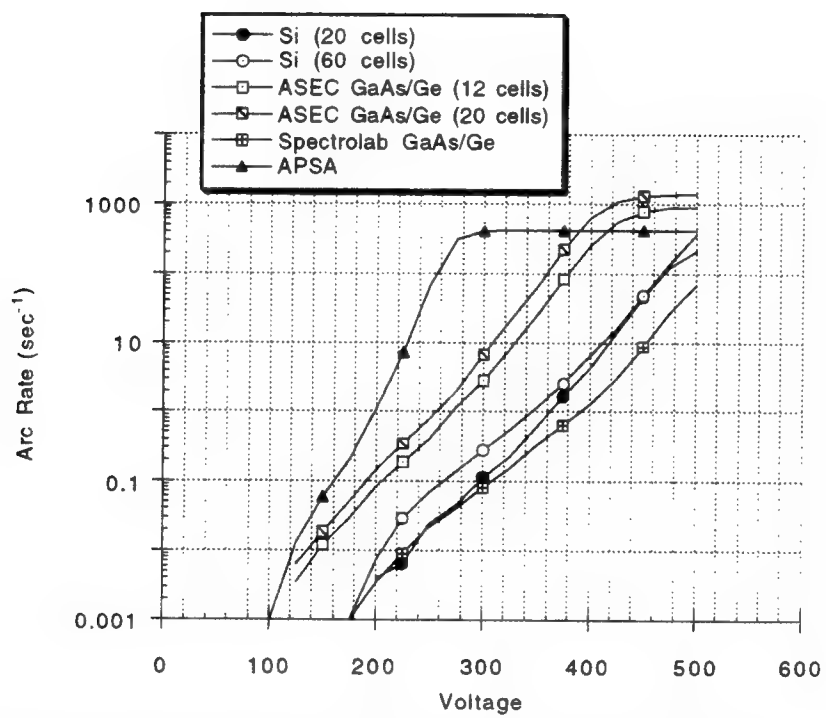


Figure 60: Arc rate prediction comparison for all PASP Plus conventional arrays at 350km

Chapter 5

Conclusions

The emergence of high voltage solar arrays has been driven by recent space system designs which require high power levels. Consequently, only recently has the negative interaction of arcing on high voltage solar arrays in low earth orbit been a concern. Since arcing can eventually destroy solar cells, it is imperative to investigate methods to reduce or even eliminate it as well as to develop methods to predict it for existing solar cells which might be used on future high voltage solar arrays. This research has addressed both of these needs.

All of the research presented in this report has been based on the numerical and analytical models discussed in Chapter 2. These models accounted for the ambient ion charging and enhanced electron field emission (EFEE) charging processes which were previously determined to be the two main factors leading to arc initiation. The numerical model simulates this arc initiation process by integrating the particle trajectories self-consistently with the dielectric surface charge. Electrons emitted from the conductor that hit the dielectric surface released secondary electrons, creating a positive surface charge which further enhances the electric field at the triple junction. With an EFEE charging site on the conductor near the triple junction, the exponential dependence of the EFEE current on the electric field causes the electric field to run away. This gives rise to arc initiation. The analytical model represents the time to arc initiation by the sum of the ambient ion charging time and the EFEE charging time. The numerical model was also modified to represent the wrap-through-contact geometry using the same charging processes. The electric field runaway, signifying arc initiation, occurs at the triple junction including the semiconductor and the coverglass. Two different dielectric charging behaviors are exhibited for relatively low and high field enhancement factors.

The models for conventional solar cells were used to determine methods of arcing mitigation in Chapter 3. Based on the analytical model, five cell properties were varied to determine their effect on the arc rate: the coverglass and adhesive dielectric thickness, the interconnector work function, the secondary electron yield, the ratio of the dielectric con-

stants, and the length of the coverglass overhang above the interconnector. The dielectric thickness was found to affect the arc rate, but significant reduction could only be attained by large thicknesses which would be costly in mass addition. The interconnector work function did not affect the arc rate much for typical metals, though very high work functions decreased the arcing rates and very low work functions increased the arcing rates at lower voltages. Secondary electron yields below unity eliminated arcing since the electric field could not run away; yields just above unity, however, did not reduce the arc rate significantly. Coverglass to adhesive dielectric constant ratios of less than unity caused the surface charge near the triple junction to remain negative for a considerably long time, thus significantly reducing the arcing rates. Overhanging the coverglass above the interconnector also caused the dielectric surface to charge negatively if the overhang was longer than the critical overhang. Overhangs less than the critical overhang only acted as thicker dielectrics with no negative surface charging. Shorter overhangs did not affect the arc rate much, but longer overhangs significantly reduced arcing rates. Therefore, arcing rates can be best reduced by increasing the dielectric thicknesses, selecting dielectric materials with coverglass to adhesive dielectric constant ratios near unity, and overhanging the coverglass above the interconnector. Dielectric secondary electron yields lower than unity will eliminate arcing at all voltages.

Arcing rates for actual solar cells were predicted in Chapter 4 for a near future space experiment, the Photovoltaic Array Space Power Plus Diagnostics (PASP Plus) experiment. Using the numerical and analytical models, the high-voltage-biased conventional cell arrays were studied. The most significant factors, which discriminated the arcing rates in the EFEE charging-dominated voltage range, were the cell thickness and number of cells in the array. As expected from the sensitivity scans, the cells with thinner dielectrics had higher arcing rates at the low voltages. In addition, the increased number of EFEE emission sites due to a higher number of cells increased the arcing rates.

Bibliography

- [1] YA. L. Al'Pert. *The Near-Earth and Interplanetary Plasma*. Vol. 1, Cambridge University Press, 1983, pp. 22-24.
- [2] M. Cho, "Arcing on High Voltage Solar Arrays in Low Earth Orbit: Theory and Computer Particle Simulation," Ph.D. Thesis, M.I.T., 1992.
- [3] M. Cho and D. E. Hastings, "Dielectric Charging Processes and Arcing Rates of High Voltage Solar Arrays", *Journal of Spacecraft and Rockets*, Vol. 28, pp. 698-706, 1991.
- [4] Ferguson D. C., "The Voltage Threshold for Arcing for Solar Cells in LEO-Flight and Ground Test Results", NASA TM-87259, March 1986.
- [5] H. Fujii, Y. Shibuya, T. Abe, K. Ijichi, R. Kasai, and K. Kuriki, "Laboratory Simulation of Plasma Interaction with High Voltage Solar Arrays", *Proceedings of the 15th International Symposium on Space Technology Science*, Kanagawa, Japan, 1986.
- [6] N. T. Grier and N. John Stevens, "Plasma Interaction Experiment (PIX) Flight Results", *Spacecraft Charging Technology 1978*, NASA CP-2071, pp. 295-314.
- [7] N. T. Grier, "Plasma Interaction Experiment II: Laboratory and Flight Results", *Spacecraft Environment Interactions Technology Conference*, 1983, NASA CP-2359, pp. 333-348.
- [8] O. Hachenberg and W. Brauer, "Secondary Electron Emission from Solids", *Advancement in Electronics and Electron Physics*, Vol. 11, pp. 413-499, 1959.
- [9] D. E. Hastings, M. Cho, and H. Kuninaka, "The Arcing Rate for a High Voltage Solar Array: Theory, Experiments and Predictions", *Journal of Spacecraft and Rockets*, Vol. 29, pp. 538-554, 1992.
- [10] D. E. Hastings, G. Weyl and D. Kaufman, "The Threshold Voltage for Arcing on Negatively Biased Solar Arrays", *Journal of Spacecraft and Rockets*, Vol. 27, pp. 539-544, 1990.

- [11] B. G. Herron, J. R. Bayless and J. D. Worden, "High Voltage Solar Array Technology", *Journal of Spacecraft and Rockets*, Vol. 10, pp. 457, 1973.
- [12] G. B. Hillard and D. C. Ferguson, "The Solar Array Module Plasma Interaction Experiment: Technical Requirements Document", NASA TM-105660, 1992.
- [13] G. B. Hillard and D. C. Ferguson, "The Solar Array Module Plasma Interactions Experiment (SAMPIE): Science and Technology Objectives", to be published in the *Journal of Spacecraft and Rockets*.
- [14] R. W. Hockney and J. W. Eastwood. *Computer Simulation Using Particles*. McGraw-Hill, USA, 1981.
- [15] G. T. Inouye and R. C. Chaky, "Enhanced Electron Emission from Positive Dielectric/Negative Metal Configurations on Spacecraft", *IEEE Trans. Nuc. Sci.*, Vol. NS-29, No. 6, December 1982, pp. 1589-1593.
- [16] G. A. Jongeward, I. Katz, M. J. Mandell and D. E. Parks, "The Role of Unneutralized Surface Ions in Negative Potential Arcing", presented at the 1985 IEEE 22nd Annual Conference, NSRE.
- [17] R. V. Latham, *High voltage Vacuum Insulation: The Physical Basis*. Academic Press, London, England, 1981.
- [18] R. V. Latham, "Prebreakdown Electron Emission", *IEEE Transactions on Electrical Insulation*, Vol. EI-18, June 1983.
- [19] P. Leung, "Characterization of EMI Generated by the Discharge of a 'Volt' Solar Array", Technical Report CR-176537, NASA, November 1985.
- [20] "PASP Plus Experiment Specification," Phillips Laboratory, US Air Force, Jan 17, 1991.
- [21] D. E. Parks, G. Jongeward, I. Katz and V. A. Davis, "Threshold-Determining Mechanisms for Discharges in High-Voltage Solar Arrays", *Journal of Spacecraft and Rockets*, Vol. 24, pp. 367-371, 1987.
- [22] D. B. Snyder, "Discharges on a Negatively Biased Solar Cell Array in a Charged Particle Environment", *Spacecraft Environment Interactions Technology Conference*, 1983, NASA CP-2359, pp. 379-388.
- [23] D. B. Snyder and E. Tyree, "The Effect of Plasma on Solar Cell Array Arc Characteristics", Technical Report TM-86887, NASA, 1985.

- [24] N. J. Stevens, "Review of Interactions of Large Space Structures with the Environment, Space Systems and their Interactions with Earth's Space Environment", *Progress in Aeronautics and Astronautics*", Vol. 71, AIAA, Washington D. C., pp. 437-454, 1980.
- [25] H. Thiemann and K. Bogus, "Anomalous Current Collection and Arcing of Solar-Cell Modules in a Simulated High-Density Low-Earth-Orbit Plasma, *ESA Journal*, Vol. 10, pp. 43-57, 1986.
- [26] H. Thieman, R. W. Schunk and K. Bogus, "Where do negatively biased solar arrays arc?", *Journal of Spacecraft and Rockets*, Vol. 27, pp. 563-565, 1990.